CMS Physics Analysis Summary

Contact: cms-pag-conveners-top@cern.ch 2017/05/15

Measurement of top quark pair-production in association with a W or Z boson in pp collisions at 13 TeV

The CMS Collaboration

Abstract

We present a measurement of the cross section of top quark pair production in association with a W or Z boson, in proton-proton collisions at a center-of-mass energy of 13 TeV at the LHC. The data sample used corresponds to an integrated luminosity of 35.9 fb^{-1}, collected in 2016 by the CMS experiment. The measurement is performed in same-charge dilepton, three- and four-lepton final states where the jet and b-jet multiplicities are exploited to enhance the signal-to-background ratio. The $t\bar{t}W$ and $t\bar{t}Z$ production cross sections are measured to be $\sigma(t\bar{t}W) = 0.80\ ^{+0.12}_{-0.11}(\text{stat.})\ ^{+0.13}_{-0.12}(\text{sys.})$pb and $\sigma(t\bar{t}Z) = 1.00^{+0.09}_{-0.08}(\text{stat.})\ ^{+0.12}_{-0.10}(\text{sys.})$pb with an expected (observed) significance of 4.6 (5.5) and 9.5 (9.9) standard deviations from the background-only hypothesis respectively. The measured cross sections are in agreement with the standard model prediction. We use these measurements to constrain the Wilson coefficients for four dimension-six operators which would modify $t\bar{t}Z$ and $t\bar{t}W$ production.

1 Introduction

The restart of the LHC at a center-of-mass energy of 13 TeV allows the study of signatures with mass scales higher than ever before. A top quark pair produced in association with a Z ($t\bar{t}Z$) or W boson ($t\bar{t}W$) are among the heaviest set of standard model (SM) particles that could be observed in the dataset accumulated so far. The Feynman diagrams for the dominant production mechanisms of these processes are shown in Fig. 1. The theoretical cross sections of the signal $t\bar{t}Z(\gamma^*)$ is 839^{+80}_{-92}(scale) $^{+25}_{-25}$(pdf) $^{+25}_{-25}(\alpha_s)$ fb and $t\bar{t}W$ is 601^{+56}_{-51}(scale) $^{+9}_{-9}$(pdf) $^{+11}_{-11}(\alpha_s)$ fb, computed at next-to-leading order (NLO) [1], and are approximately 3-4 times higher than the production rates for 8 TeV pp collisions. The precise measurement of these processes is of particular interest as they are dominant backgrounds to several searches for new physics. Furthermore, the $t\bar{t}Z$ production is the most sensitive process for direct measurement of the couplings of the top quark and the Z boson.

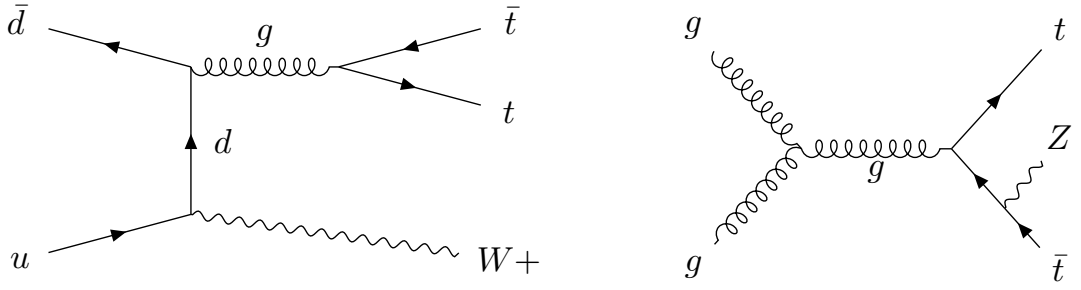

Figure 1: The leading order Feynman diagram for $t\bar{t}Z$, $t\bar{t}W$ production at the LHC. The charge conjugate of the diagrams shown is implied.

The $t\bar{t}Z$ cross section was first measured by the CMS experiment [2] in 7 TeV collisions, with a precision of about 50% [3]. More recent measurements of the $t\bar{t}W$ and $t\bar{t}Z$ cross sections, in events containing two, three, or four leptons, in 8 TeV collisions at CMS used elaborate multivariate techniques and constrained $\sigma(t\bar{t}W)$ and $\sigma(t\bar{t}Z)$ to within 30% and 25% of their SM values respectively using a dataset of 19.5 fb^{-1} [4, 5]. The $t\bar{t}Z$ process was observed with a significance of 6.4 standard deviations (σ) and evidence for $t\bar{t}W$ production was found with 4.8 σ significance. The ATLAS experiment analyzed events containing two and three leptons for the $t\bar{t}W$ cross-section measurement and two, three and four leptons events for the $t\bar{t}Z$ cross-section measurement, achieving a similar precision [6]. ATLAS also reported a measurement of the $t\bar{t}W$ and $t\bar{t}Z$ production cross sections in multilepton final states, $\sigma(t\bar{t}W) = 1.5 \pm 0.8$ pb and $\sigma(t\bar{t}Z) = 0.9 \pm 0.3$ pb, using 3.2 fb^{-1} of 2015 data at a center of mass energy of 13 TeV [7].

In this document, we present a new measurement of the $t\bar{t}Z$ and $t\bar{t}W$ production cross-sections at 13 TeV with data corresponding to an integrated luminosity of 35.9 fb^{-1}. The measurements are performed using events in which at least one of the W bosons originating from a top quark decays to a lepton and a neutrino, and the associated W(Z) boson decays to a lepton and neutrino (lepton pair), where a lepton (ℓ) refers to an electron or a muon. Decays to τ leptons are included through its leptonic decays. The collision events are analysed in three exclusive final states: events with two same-charge leptons are used to extract the $t\bar{t}W$ signal, while the events with three leptons or four leptons with a lepton pair of same flavour and opposite charge (SFOC) are used for obtaining $t\bar{t}Z$ signal counts. In addition to individual $t\bar{t}W$ and $t\bar{t}Z$ cross-sections measurements, a two dimensional fit is performed for these cross-sections using the results of all three analyses.

2 Event samples and object selection

This analysis uses proton-proton collision data corresponding to an integrated luminosity of 35.9 fb^{-1} collected in 2016 by the CMS detector. Collision events are selected by online triggers that require the presence of at least one electron or one muon, with transverse momentum (p_{T}) greater than 27 and 24 GeV respectively. Efficiencies of the trigger selection for signal and background events that pass the full event selection are found to be greater than 95% for the dilepton analysis, and greater than 98% for the three- and four-leptons analyses.

Monte Carlo generators are used to estimate some of the backgrounds, as well as to calculate the selection efficiency for the $\mathrm{t\bar{t}Z}$ and $\mathrm{t\bar{t}W}$ signal events.

The simulated samples for the $\mathrm{t\bar{t}}$ and $\mathrm{W}\gamma^*$ processes are generated at leading order (LO) with the MADGRAPH 5 generator [8] and those for $\mathrm{t\bar{t}Z}$, $\mathrm{t\bar{t}W}$, tZq, tHq, tHW, WZ, tWZ, WWZ, WZZ, ZZZ, $\mathrm{t\bar{t}}\gamma$ and $\mathrm{Z}\gamma^*$ processes are generated at next-to-leading order (NLO) with MG5_AMC@NLO [9], except for tWZ, which is generated at leading order. Parton showering, hadronization and the underlying event are simulated using PYTHIA v8.2 [10, 11]. The NLO POWHEG v2 [12, 13] generator is used for the production of the $\mathrm{t\bar{t}H}$ and $\mathrm{q\bar{q}}\rightarrow\mathrm{ZZ}$ processes, while the $\mathrm{gg}\rightarrow\mathrm{ZZ}$ process is generated at leading order with MCFM [14]. The simulated samples for ZZ are scaled to correspond to cross sections calculated at next-to-next-to-leading order (NNLO) for $\mathrm{q\bar{q}}\rightarrow\mathrm{ZZ}$ [15] (scaling K factor 1.1) and at NLO for $\mathrm{gg}\rightarrow\mathrm{ZZ}$ [16] (scaling K factor 1.7). All generated events are processed and reconstructed by a GEANT4-based model [17] of the CMS detector. Simultaneous pp collisions per bunch-crossing, so-called pileup (PU), are simulated in addition to the hard-scattering process. The simulated pileup multiplicity matches that estimated in the data.

The theoretical cross section of the signal $\mathrm{t\bar{t}W}$ and $\mathrm{t\bar{t}Z}(\gamma^*)$ is computed at NLO with MG5_AMC@NLO. For $\mathrm{t\bar{t}Z}(\gamma^*)$ the invariant mass of any two leptons is required to be greater than 10 GeV. In both cases all decay channels of W, Z and γ^* are included.

The offline event reconstruction uses the CMS particle-flow (PF) algorithm [18] for particle reconstruction and identification.

Leptons are required to have $p_{\mathrm{T}} > 10\,\text{GeV}$ and $|\eta| < 2.5$ (2.4) for electrons (muons). For each electron (muon) candidate, a cone of $\Delta R < 0.3$ (0.4) is constructed around the track direction at the event vertex. ΔR is defined as $\sqrt{(\Delta\eta)^2 + (\Delta\phi)^2}$, where $\Delta\eta$ and $\Delta\phi$ are the distances in pseudorapidity and azimuthal angle from the lepton track. The scalar sum of the p_{T} of all particles reconstructed with the PF algorithm within the cone, which are consistent with the selected primary vertex of the event, is calculated, excluding the contribution from the lepton candidate. The average energy density deposited by neutral particles in the event, computed with the FastJet [19, 20] program, is used to subtract the contribution from neutral particles to the sum of the p_{T} of particles in the cone. The relative isolation discriminant, I_{rel}, is then defined as the ratio of this sum to the p_{T} of the lepton candidate. An electron candidate with a calorimetric energy deposit in the ECAL is selected if $I_{\mathrm{rel}} < 0.1$ for all three analyses and a muon candidate is selected if $I_{\mathrm{rel}} < 0.25$ for three- and four-lepton analyses, while for the same-charge dilepton analysis $I_{\mathrm{rel}} < 0.15$ is used. Consistency of the track with the selected primary vertex is enforced by vetoing lepton candidates with a transverse and longitudinal displacement from the primary collision vertex of more than 0.05 cm and 0.1 cm respectively. Additionally, the transverse track impact parameter significance is required to be larger than 4, where the impact parameter is the minimum three-dimensional distance between the lepton trajectory and the primary vertex and its significance is the ratio of the impact parameter to its uncertainty.

Jets are reconstructed by clustering PF candidates using the anti-k_{T} algorithm [21] with a dis-

tance parameter of $R = 0.4$. The influence of PU is mitigated using the charged hadron subtraction technique, which removes the energy of charged hadrons not coming from the primary vertex [22]. Missing transverse momentum ($E_{\mathrm{T}}^{\mathrm{miss}}$) is computed as the magnitude of the vector sum of all PF candidate transverse momenta.

Jets are calibrated in simulation and in data separately, accounting for deposits from PU and the non-linear detector response. Calibrated jets with $p_{\mathrm{T}} > 30$ GeV and $|\eta| < 2.4$ are selected. Furthermore jets formed with fewer than three PF candidates, or with electromagnetic or hadronic energy fractions greater than 99% are vetoed. A selected jet may still overlap with the selected leptons leading to a double-counting. To prevent such cases, jets that are found within a cone of $R = 0.4$ around any of the signal leptons are removed from the set of selected jets.

The multivariate b-tagging discriminator "Combined Secondary Vertex Tagger" [23] is used to identify jets that originate from hadronization of b quarks. The selection criteria that is used has a mistag rate of the order of 1% and a corresponding tagging efficiency of approximately 70% depending on the jet transverse momentum and pseudorapidity.

3 Event Selection

3.1 Same-Charge Dilepton Analysis

We measure the production rate of $\mathrm{t\bar{t}W}$ events in a channel with exactly two same-charge leptons that targets the following decay mode:

$$\mathrm{pp} \to \mathrm{t\bar{t}W} \to (\mathrm{t} \to \mathrm{b}\ell\nu)(\mathrm{t} \to \mathrm{b}jj)(\mathrm{W} \to \ell\nu) \tag{1}$$

where b and j refer to jets formed by bottom- and light-flavour quarks respectively. By requiring the same charge for the two light leptons only one third of the signal produced in the dilepton final state is expected to be selected. However, this selection significantly improves the signal over background ratio, as prompt same-charge lepton pairs are produced in SM processes with relatively small cross sections. The main backgrounds to this analysis are due to misreconstruction effects: misidentification of nonprompt leptons from heavy flavour meson decays, hereafter called nonprompt leptons as opposed to those prompt leptons originating from W/Z decays, and mis-measurement of the charge of one of the leptons in events with an opposite charge lepton pair. In order to distinguish these backgrounds from the signal, a multivariate analysis (MVA) has been developed.

We select events with exactly two same-charge leptons ($\mu\mu$, μe, ee) where both the leading and the trailing lepton transverse momenta are required to be above 25 GeV. To increase the trigger selection efficiency, in the ee channel the leading electron is additionally required to fulfill $\mathrm{p_T} > 40$ GeV. Events containing additional leptons passing looser identification and isolation requirements are vetoed. This set of loose identification and isolation criteria is the same as the one used to estimate the non-prompt background from data (see Sec. 4).

The MVA has been trained using events from $\mathrm{t\bar{t}W}$ signal and background samples which are selected if they contain at least two jets and one or more b-jets. The invariant mass of SFOC leptons must be greater than 12 GeV. In order to suppress $\mathrm{Z} \to e^+e^-$ events, the invariant mass of the two electrons is required to lie outside a 15 GeV window around the Z pole mass [24] and $E_{\mathrm{T}}^{\mathrm{miss}} > 30$ GeV is required.

Among the several kinematic observables that were examined as inputs to the multivariate analysis training, the following variables are found to provide the best discrimination between

the signal and background: the number of jets, N_{jets}; number of b-jets, $N_{\text{b jets}}$; the scalar sum of p_{T} of the jets, H_{T}; the missing transverse energy, $E_{\text{T}}^{\text{miss}}$; the leading and the trailing lepton p_{T}; the transverse mass of each of the leptons and missing transverse energy; the leading and subleading jet p_{T}; and ΔR between the trailing lepton and the nearest selected jet.

A Boosted Decision Tree (BDT) classifier with a gradient boost [25] was used and simulated events were equally split for training and testing. Figure 2 shows the kinematic distributions of variables used in the MVA and Fig. 3 shows the output of the BDT classifier in all background sources and the signal scaled to the integrated luminosity of the analyzed data samples.

Events with BDT value > 0 were selected to suppress the background due to nonprompt leptons and for the final signal extraction these events were split into two categories: $0 <$ BDT value < 0.6, BDT value > 0.6. These values were optimised to achieve the best expected sensitivity for $\text{t}\bar{\text{t}}\text{W}$. Furthermore, the number of jets and b-jets are used to form five exclusive event categories to maximize the signal significance. These categories are constructed with events using two jets; three, and four or more jets. The latter two categories are further split according to the number of b jets, $N_{\text{b jets}} = 1, \geq 2$. Events with BDT value < 0 are also used in the signal extraction procedure in order to constrain the uncertainties on the non-prompt lepton background.

Each of these categories are further split into two separate sets according to the charge of the leptons; $++$ or $--$. This increases sensitivity due to the charge asymmetric production of the signal ($\text{t}\bar{\text{t}}\text{W}^{+}$ vs $\text{t}\bar{\text{t}}\text{W}^{-}$) resulting from the proton-proton nature of the collision at the LHC, while backgrounds are expected to yield charge symmetric dileptons. In total 20 exclusive signal regions are formed.

3.2 Three Lepton Analysis

We measure the production rate of $\text{t}\bar{\text{t}}\text{Z}$ events in a channel with exactly three leptons that targets the following decay mode:

$$\text{pp} \to \text{t}\bar{\text{t}}\text{Z} \to (\text{t} \to \text{b}\ell^{\pm}\nu)(\text{t} \to \text{bjj})(\text{Z} \to \ell^{\pm}\ell^{\mp}) \tag{2}$$

We select events that contain exactly three leptons ($\mu\mu\mu$, $\mu\mu e$, μee and eee) where the leading, subleading and trailing lepton p_{T} are required to be above 40, 20 and 10 GeV, respectively. In order to reduce backgrounds from multilepton processes that do not contain a Z boson, we require the invariant mass of two SFOC leptons, $\text{M}(\ell\ell)$, to be consistent with the Z boson hypothesis, namely $|\text{M}(\ell\ell) - \text{M}_{\text{Z}}| < 10\,\text{GeV}$.

Signal events are expected to have at least four jets, two of which originate from b-quarks. In the case where all of these pass the jet and b jet requirements defined in the previous section, one obtains a sample of events that is enriched by the signal with a minimal background contribution. However, nearly 70% of the signal events fail to pass the requirement on all four jet and two b jet requirements. We therefore make use of the jet and b jet multiplicities to form nine exclusive event categories to exploit all the signal events. These nine categories are formed using events with $N_{\text{jets}} = 2$, $N_{\text{jets}} = 3$ and $N_{\text{jets}} \geq 4$, where each jet multiplicity bin gets further split according to $N_{\text{b jets}} = 0$, 1 and ≥ 2.

Despite the larger background contamination, the $N_{\text{jets}} = 3$ categories, in particular the higher $N_{\text{b jets}}$ bins, improve the signal sensitivity, as this category recovers signal efficiency for the cases where one of the jets fall out of acceptance. The $N_{\text{jets}} = 2$ category provides a background-dominated region which helps to constrain the background uncertainties. We use all nine signal

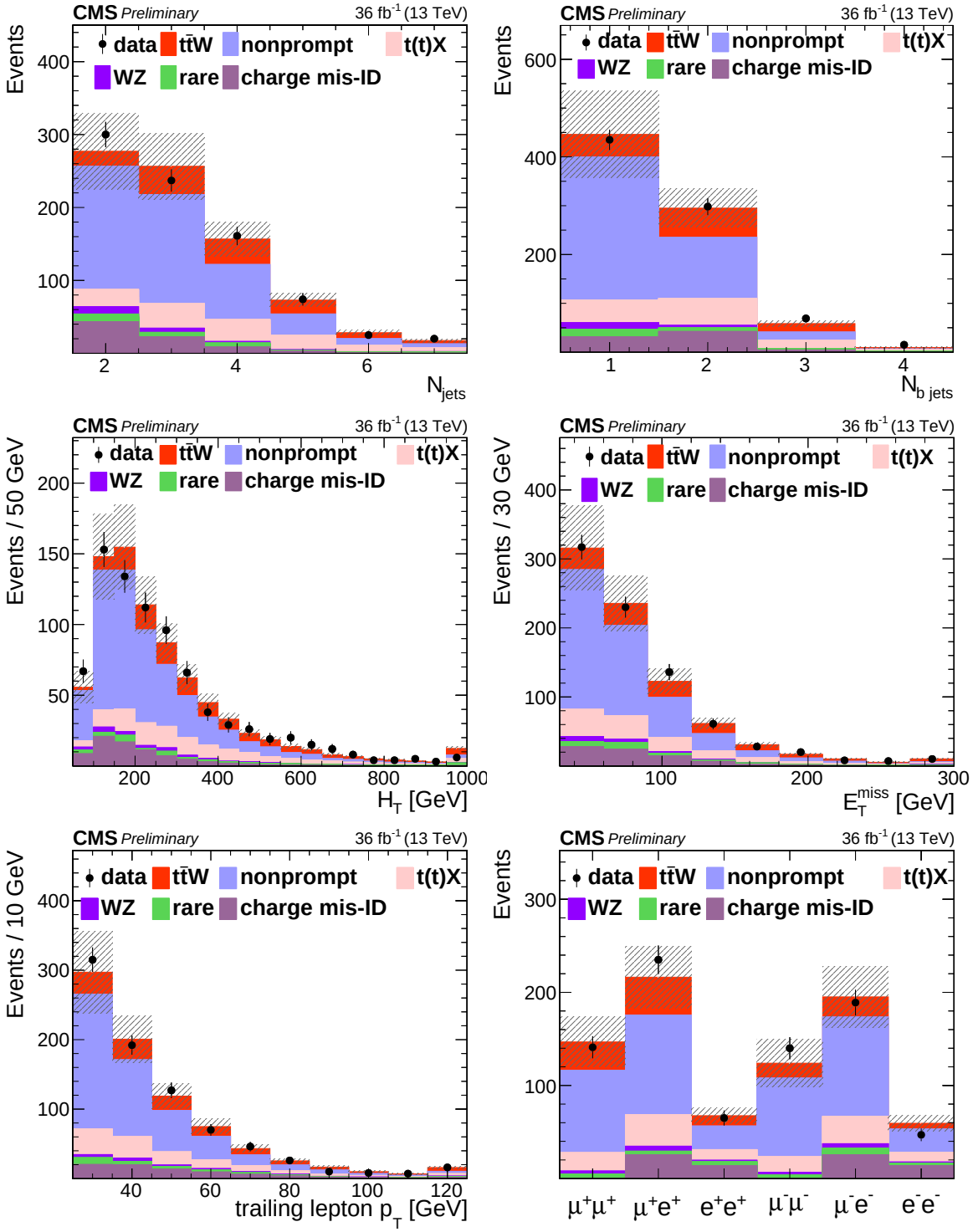

Figure 2: Distribution of different kinematic variables in data compared to the estimated expectations. From left to right: jet multplicity and b-jet multiplicity (top), H_T and E_T^{miss} (center), trailing lepton p_T and event yields (bottom). The expected contribution from the different background processes are stacked as well as the expected contribution from the signal. The shaded band represents the uncertainty in the prediction of the background and the signal processes.

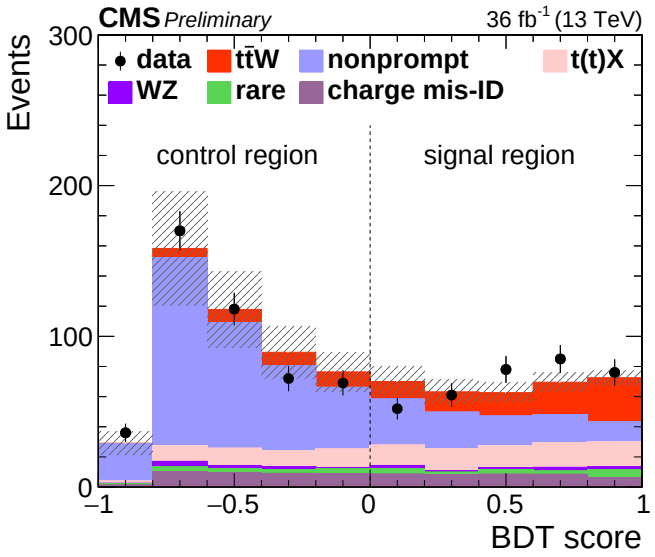

Figure 3: BDT value distribution for background and signal processes. The expected contribution from the different background processes are stacked as well as the expected contribution from the signal. The shaded band represents the uncertainty in the prediction of the background and the signal processes.

regions to extract the signal significance and the cross section.

3.3 Four Lepton Analysis

The analysis of $\mathrm{t\bar{t}Z}$ with four-lepton final states aims to select events produced in the process

$$\mathrm{pp} \to t\bar{t}Z \to (t \to bW^{+} \to b\ell^{+}\nu)(\bar{t} \to \bar{b}W^{-} \to \bar{b}\ell^{-}\bar{\nu})(Z \to \ell^{\pm}\ell^{\mp}) \tag{3}$$

The events are characterized by the presence of two b jets, missing energy and four prompt leptons, two of which form a SFOC pair consistent with the Z boson mass. Due to the small branching ratio of $\mathrm{t\bar{t}Z}$ to 4 leptons, the event selection is optimized to obtain high signal efficiency in simulation. The following selection steps are implemented. Events with exactly four leptons, which pass the lepton identification and isolation selection described in Sec. 2, are selected. The highest lepton p_{T} is required to be greater than 40 GeV, the p_{T} of the remaining three leptons is required to be greater than 10 GeV. The sum of the lepton charges should be zero, and the invariant mass of any lepton pair is required to be greater than 12 GeV. At least one SFOC lepton pair with an invariant mass $|\mathrm{M}(\ell\ell) - \mathrm{m_Z}| < 20$ GeV should be present in the event. Events with $\mu\mu\mu\mu$, $eeee$ and $\mu\mu ee$ final states, where a second SFOC lepton pair consistent with the Z boson mass is found, are rejected. Furthermore, at least two jets and at least one b jet is required. Two sets of events are used for signal extraction: events passing all selection steps (high signal-to-background ratio category), and events passing all steps except the b jet requirement (low signal-to-background ratio category).

4 Background predictions

4.1 Background due to nonprompt lepton

Nonprompt leptons, i.e. leptons from heavy-flavour hadron decay, misidentified hadrons, muons from light-meson decays, or electrons from unidentified photon conversions, are rejected by the

identification and the isolation criteria applied on electrons and muons. Nonetheless, a residual background from such leptons leaks into the analysis selection. In this analysis such backgrounds are mainly expected to come from top quark pair production, where one or two of the leptons originate from the leptonic W boson decays and an additional nonprompt lepton from the semileptonic decays of a b hadron, and in $Z \to \ell\ell$ events with an additional misidentified nonprompt lepton. These backgrounds are estimated using a data-driven technique. Using a control sample in data, we calculate the probability for a loosely identified nonprompt lepton to also pass the full set of tight requirements, designated as the tight-to-loose ratio. For loose leptons a relaxed isolation requirement ($I_{\text{rel}} < 1$) is chosen, and additional electron identification requirements on variables (e.g. the ratio of the energy measured in the electromagnetic calorimeter to the energy measured in the hadron calorimeter) that distinguish true electrons from hadrons and photons are relaxed. The tight-to-loose ratios are measured in a data control sample of QCD multijet events that are enriched in nonprompt leptons. This control sample consists of events with a single lepton and at least one jet, where the lepton and jets are separated by $\Delta R > 1$. We suppress the prompt lepton contamination, mostly due to W+jets, by applying an upper cut on the missing transverse energy, $E_{\text{T}}^{\text{miss}} < 20$ GeV, as well as on the transverse mass, M_{T}, which is the invariant mass calculated using only the transverse component of momentum vector of the lepton and $E_{\text{T}}^{\text{miss}}$. The residual prompt lepton contamination is subtracted using estimates from MC simulations. This subtraction is relevant only for the high p_{T} leptons and its effect on the total estimated background does not exceed a few percent. These probabilities are parametrised as functions of the pseudorapidity of the leptons and p_T^{Cor}. The p_T^{Cor} variable is calculated by correcting the lepton p_{T} as a function of the energy in the isolation cone around it. This definition leaves the p_{T} of the leptons passing the isolation cut unchanged and modifies the p_{T} of those failing the cut so that it is a better proxy for the mother parton p_{T} [26]. The measured probabilities in data vary from 5% to 30%, where higher values correspond to the low lepton p_{T} region. These measured probabilities are then used to extrapolate the number of nonprompt leptons passing the selection requirements from a sample of side-band events which satisfies all the analysis requirements except that at least one of the leptons does not pass the tight selection but passes the loose selection. Each event in this region is assigned a weight picked from the tight-to-loose ratio map, according to the p_{T} and η of the loose lepton.

We validate this technique with simulated events. The tight-to-loose ratios are first measured for electrons and muons in QCD MC events, and then applied in $\text{t}\bar{\text{t}}$ and Z+jets MC events in exactly the same way as is done in data to obtain predictions for nonprompt background contamination. These predictions agree very well with the observed yields in simulation. Based on these validations we assign a 30% systematic uncertainty to the predicted nonprompt lepton background. Additionally, data control regions, exclusive to the signal extraction region and enriched by the processes with nonprompt leptons, are formed to check any other potential source of uncertainties. For the same-charge dilepton channel the region with BDT < 0 is used. Figure 4 shows the predicted background and observed data yields versus N_{jets} and the p_{T} of the trailing lepton. For three lepton channel this control region is defined by either the absence of an SFOC lepton pair or with an SFOC pair with an invariant mass away from the Z boson mass by at least 10 GeV and at least one tagged jet. This region is dominated by $\text{t}\bar{\text{t}}$ events where both W bosons decay leptonically and an additional nonprompt lepton is present. Figure 5 shows the predicted and observed yields versus flavour of the leptons, $E_{\text{T}}^{\text{miss}}$, N_{jets} and $N_{\text{b jets}}$. Both of these control regions show very good agreement between predicted and observed yields.

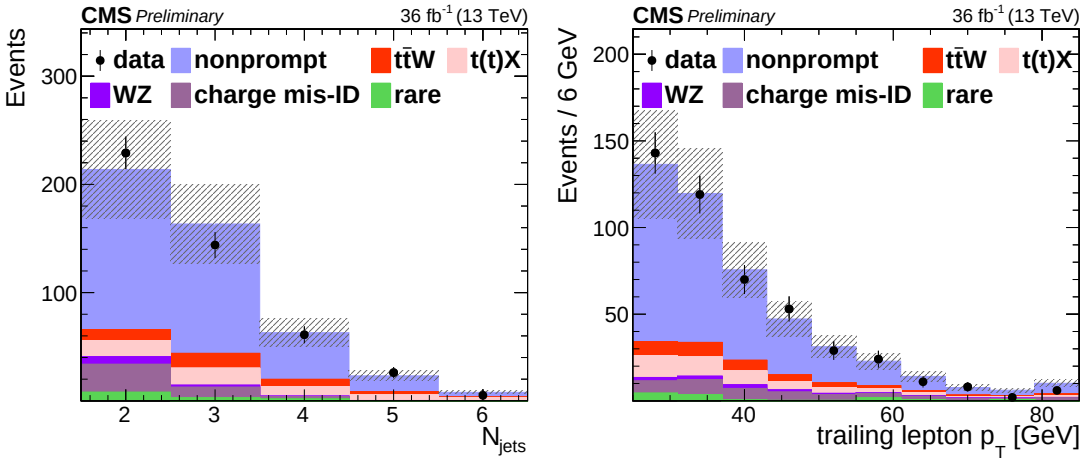

Figure 4: Nonprompt control region plots in dilepton channel with BDT < 0: distributions of the total yields versus jet multiplicity and transverse momentum of the trailing lepton.

4.2 Background due to WZ production

Kinematic distributions for the background due to WZ production are taken from simulation. This background has the highest expected yields in the analysis region with no b-tagged jets. The data used for this analysis contains a substantial number of WZ events that can be isolated and compared with the MC predictions. We define a control region in a sub-set of the data with the following requirements. Events with exactly three leptons with the same p_{T} thresholds as the ones used in the $\mathrm{t\bar{t}Z}$ selection, where two leptons form a SFOC pair with $|\mathrm{M}(\ell\ell) - \mathrm{m_Z}| < 10$ GeV, with less than two jets, and no b-tagged jets are selected. Additionally $E_{\mathrm{T}}^{\mathrm{miss}}$ is required to be greater than 30 GeV, and the transverse mass constructed using the lepton that is not used for $\mathrm{M}(\ell\ell)$ calculation with the $E_{\mathrm{T}}^{\mathrm{miss}}$, M_{T}, is required to be greater than 50 GeV.

With this selection we obtain a data sample that is expected to be 85% pure in WZ events. Figure 6 shows the number of events in each lepton flavour channel and the N_{jets}, M_{T} and the $\mathrm{M}(\ell\ell)$ distributions. The expected background from nonprompt leptons is measured from data using the method described above. The other background ($t(t)X$ and rare SM processes) contributions are obtained from simulated samples. We observe an overall reasonable agreement between data and the total expectation in all four lepton channels and also in the kinematic distributions. The ratio of the observed to predicted yields is found to be 0.94 ± 0.07 where the uncertainty is statistical. With this level of agreement between data and the MC prediction, we proceed without applying a scale factor to the WZ prediction obtained by MC, and use it to assess the systematic uncertainty on the WZ background prediction. We also study possible mis-modelling of the WZ plus heavy-flavour background at high b jet multiplicities. We find that WZ contribution at high b jet multiplicities is mainly caused by the misidentification of light-flavour jets as bjets. The WZ+b quark content is checked in MC and in all analysis categories it varies between 5% and 15%. In order to take into account the differences in b-tagging efficiencies and misidentification probabilities in data and simulation, scale-factors are applied [23]. With all these corrections applied, we check the agreement between data and Z+jets MC as a function of b jet multiplicity in SFOS dilepton events consistent with the Z boson mass. Based on this study, we assign a 10% systematic uncertainty to the WZ background estimation, which covers the differences between data and expectations found in the control region. Additional uncertainties associated with the extrapolation from this control region to high jet (b jet) multiplicity regions, such as jet energy scale and b tagging uncertainties, are considered separately.

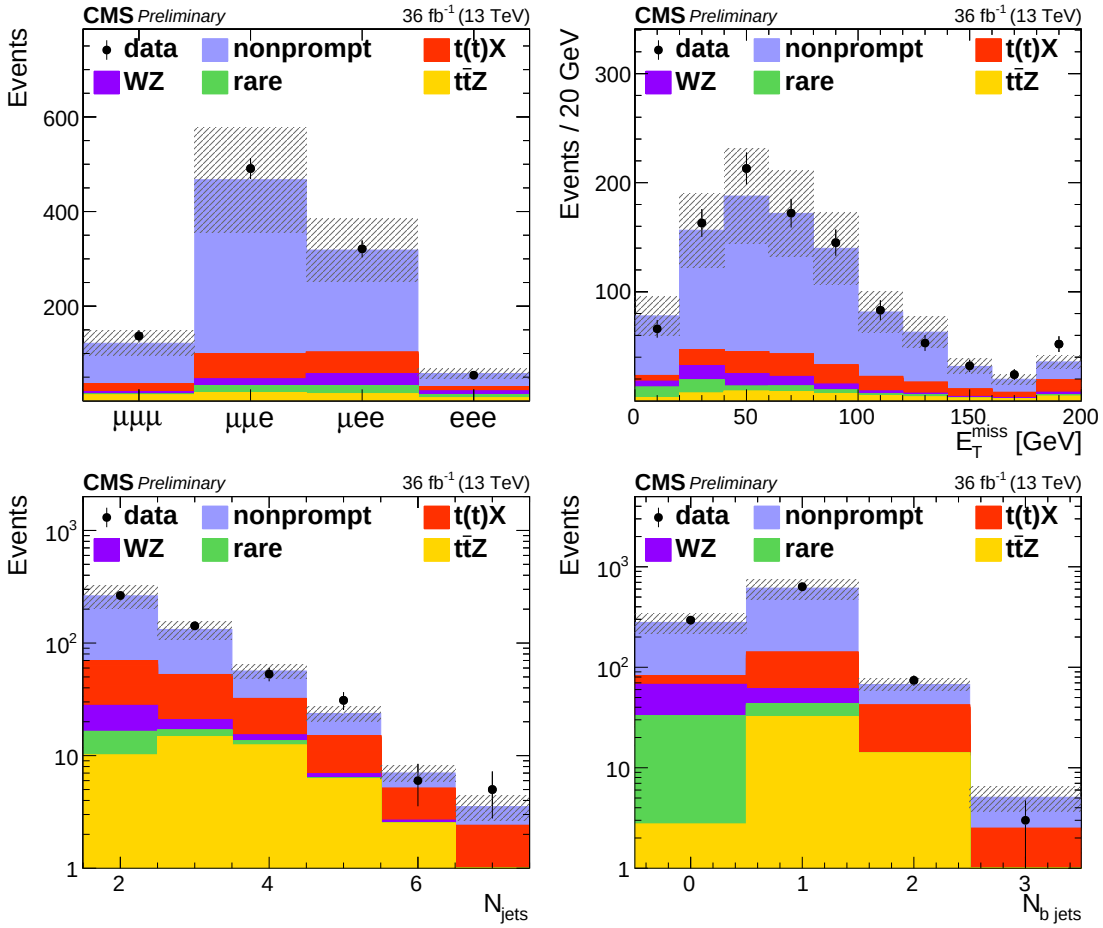

Figure 5: Nonprompt control region plots in trilepton channel: distributions of the total yields versus lepton channel, missing transverse energy and (b-tagged) jet multiplicity.

4.3 Background due to $t(t)X$ and rare SM processes

The background events containing either multi-bosons or top quark(s) in association with a W, Z or Higgs boson are estimated from simulation scaled by their NLO cross section and normalised to the integrated luminosity. The following backgrounds contribute to this category:

- $t(t)X$: $t\bar{t}H$, tWZ, tqZ, tHq, tHW, tttt with 2 or 3 prompt leptons.
- Rare: ZZ, $Z\gamma^*$, WZZ, ZZZ with three or four prompt leptons, where one of the four leptons escapes detection.

For background yields in the "$t(t)X$ " category we studied the theoretical and systematic uncertainties separately. The theoretical uncertainties for the inclusive cross section for these processes are around 10% [27–29]. Using the simulations we study the effect of the renormalisation and factorisation scale variations as well as the uncertainties due to PDF choices in the phase-space region relative to this analysis. From these studies we deduce a conservative theoretical uncertainty of 2%. On the experimental side, in order to account for the differences in the lepton selection efficiencies, b jet identification efficiencies as well as false b-tagging rate between the simulation and the data, we apply scale factors to the predictions obtained from MC, and we assign systematic uncertainties associated with these scale factors. These experimental uncertainties are estimated in each analysis category (see Sec. 5) and are applied in addition to the above mentioned 2%.

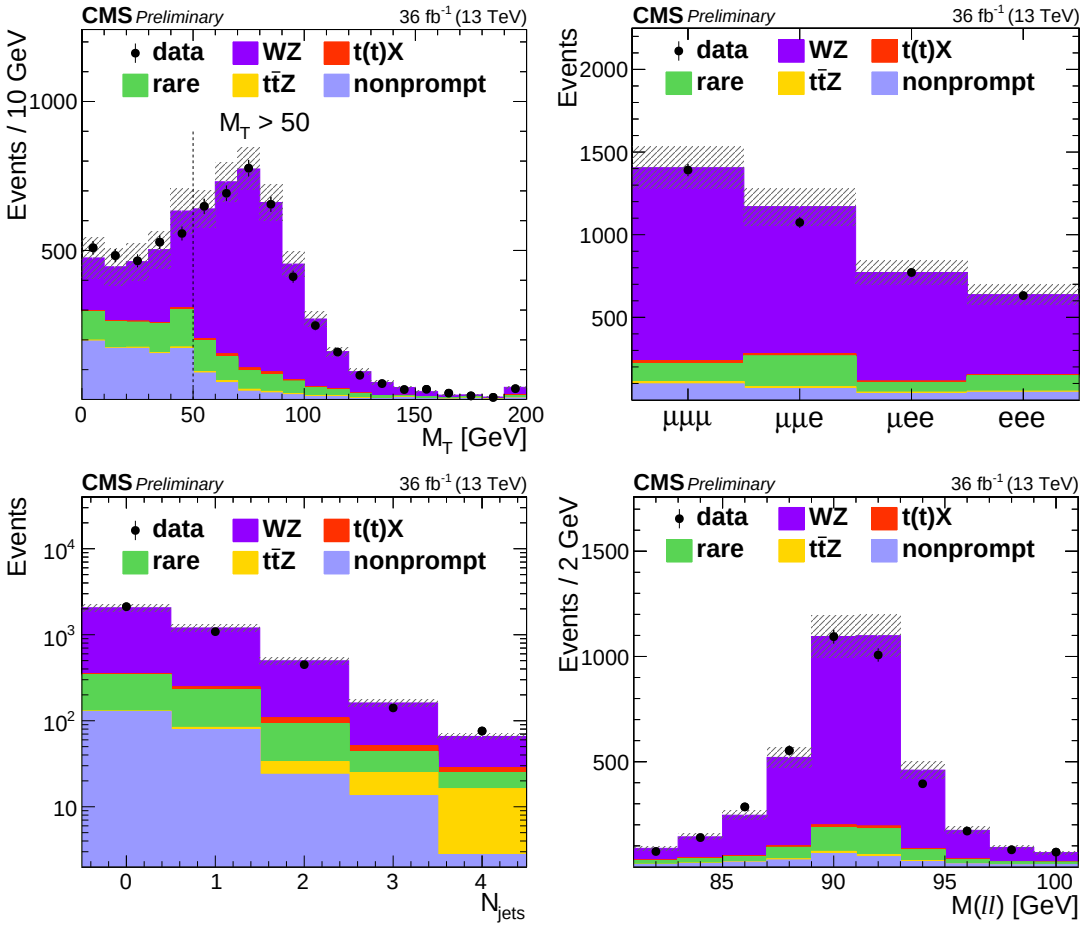

Figure 6: WZ control region plots: Distributions of the total yields versus lepton channel, jet multiplicity, transverse mass of the lepton and the missing transverse energy and the reconstructed invariant mass of the Z boson candidates. For all the plots the requirement on jet multiplicity is suppressed.

The rate for the backgrounds from rare SM processes, except ZZ, are assigned an overall 50% systematic uncertainty. This is motivated by the fact that these processes are not yet measured at the LHC and the uncertainties associated with the absence of higher order effects might be large in the phase-space relevant to this analysis. For the ZZ background the consistency between data and simulation is validated in a ZZ-dominated background region. The events are selected following the first four steps, mentioned in Sec. 3.2, in the selection sequence and requiring two SFOC lepton pairs with an invariant mass within a 20 GeV window around the Z mass. Control plots comparing data and simulation are shown in Fig. 7. The ZZ control region, which is >95% pure in ZZ, shows good agreement between data and simulation in events with extra jets.

For the ZZ background, based on the study in the four-lepton control region, as well as considering the studies done for the WZ background, a 20% systematic uncertainty is assigned. Additional experimental uncertainties, as previously described for the $t(t)X$ and WZ backgrounds, are also considered to apply to the ZZ background.

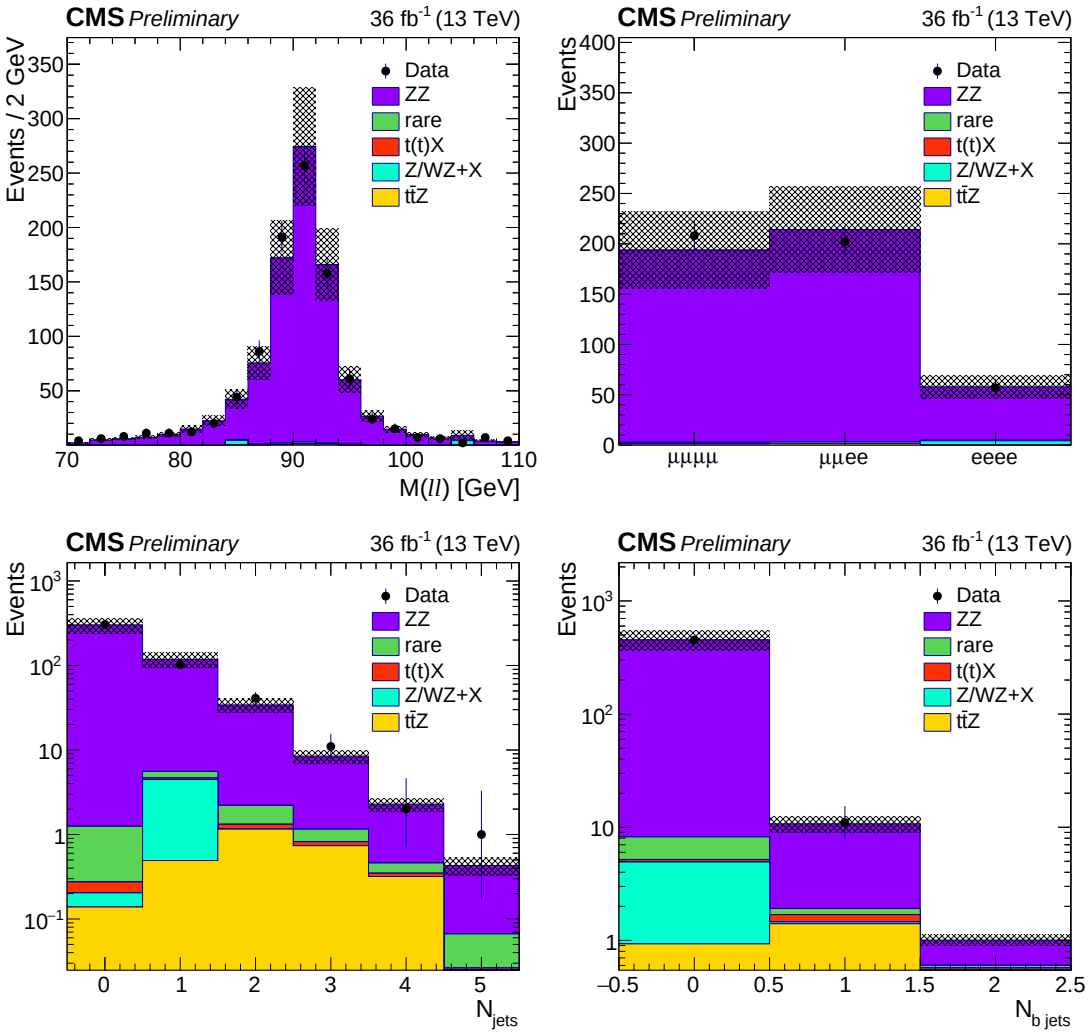

Figure 7: Data-MC comparison for the Z candidates mass (top left), event yields (top right), jet multiplicity (bottom left) and b-jet multiplicity (bottom right) in a ZZ-dominated background control region

4.4 Background induced by the mismeasurement of the lepton charge

The background due to charge mis-measurement is estimated by selecting opposite-charge ee or $e\mu$ data events passing the full kinematic selection and then weighing them by the p_{T} and η dependent probability of electron charge misidentification. This probability is obtained from MC simulation.

The charge mis-measurement rate in simulation is validated in data by comparing the simulation result with the measured values in data. The charge misidentification rate is measured in Drell-Yan (DY) events in MC and in data where events with two same charge electrons with an invariant mass that fall within a Z mass window $76 < \mathrm{M}(\ell\ell) < 106$ GeV are selected. The measured electron charge misidentification rates in data and in DY simulation are in a good agreement and varies from $4 \cdot 10^{-5}$ for barrel low p_{T} electrons to $4 \cdot 10^{-3}$ for endcap high p_{T} electrons.

The physics process contributing to this category of background in signal regions is primarily top-pair production. Based on the data-MC agreement for the charge mis-measurement rate

and the potential differences between the measurement described here and the one in the $\bar{\mathrm{t}}\mathrm{t}$ process we assign a 20% systematic uncertainty on this background prediction.

5 Signal acceptance and systematic uncertainties

The uncertainty on the integrated luminosity is 2.5% [30]. Simulated samples are reweighed according to the distribution of the true number of interactions at each bunch crossing. The uncertainty on the total inelastic pp cross section, which affects the PU estimate, is 5% and leads to 1-2% uncertainty on the expected yields.

We measure the trigger efficiencies in a data sample that is orthogonal to the signal selection and in simulation. These efficiencies are measured for each channel separately and parametrised as a function of lepton p_{T} and pseudorapidity. The overall efficiency for the same-sign dilepton analysis is higher than 95%; for the three- and four-lepton analyses it is greater than 98%. The trigger efficiencies measured in simulation agree with the one measured in data within 1%, with an exception in the dimuon channel, where the difference reaches to 3%. The event yields in simulation are scaled to match the trigger efficiencies in data. We assign 2-4% uncertainty depending on the channel due to these scale factors.

Reconstructed lepton selection efficiencies are measured with a tag-and-probe method [31, 32] in bins of p_{T} and pseudorapidity of leptons, and are higher than 65 (96)% for electrons (muons). These measurements are performed separately in data and in simulation. The differences between these two measurements are typically around 1-4% per lepton, which amount to 3-7% when added up for all leptons in the event.

Uncertainties in the jet energy calibration are estimated by shifting the energy of jets in the simulation up and down by one standard deviation. Depending on transverse momentum and pseudorapidity, the uncertainty in the jet energy scale is 2-5%. The observed differences between the varied and the original results are taken as uncertainty for the background components, which are taken from simulation, and signals. The same technique is used to calculate the uncertainties caused by the jet resolution, for which the uncertainity is found to be 1-6%. The b-tagging efficiency in the simulation is corrected using scale factors determined from the data [33]. These contribute an uncertainty of about 2-5% on the predicted yields depending on transverse momentum, pseudo-rapidity and jet and b-tag multiplicity.

In order to estimate the theoretical uncertainties from renormalisation and factorisation scales they are each varied independently up and down by a factor of 2, where the anti-correlated variations are dropped. For the acceptance uncertainties, the envelope of the variations is used as an uncertainty in each search bin and does not exceed 2%. The different replicas in the NNPDF30 PDF set [34] are used to estimate the corresponding acceptance uncertainty which typically amounts to less than 1%.

For the contribution from top quark (pair) production in association with a Higgs and vector boson we assess an uncertainty of 11% on the cross section. For the WZ and ZZ backgrounds, with cross-checks in data, the uncertainty is 10% and with additional uncertainties at large jet multiplicities. Rare SM processes are assigned a 50% systematic uncertainty. All of the experimental uncertainties described above are evaluated for each process in all analysis categories. A 20% systematic uncertainty is assigned to the charge mis-identification background. The uncertainty on the nonprompt lepton contribution in the same-sign dilepton and three-lepton analyses is 30% where the statistical uncertainty in the side bands is also taken into account, while the four-lepton analysis includes a conservative 100% uncertainty on this background.

The theoretical uncertainties for individual backgrounds as well as the systematic uncertainties for the nonprompt background prediction are uncorrelated to each other, but correlated across the analysis categories. The different sources of experimental uncertainty are correlated across the analysis categories and between the backgrounds and signal predictions. The statistical uncertainties due to the limited MC statistics and the data events in the sideband region in data-driven background are considered fully uncorrelated.

The impact of different sources of systematic uncertainty is estimated by fixing the nuisance parameter's uncertainty one at a time and evaluating the decrease in the total systematic uncertainty. Uncertainties on the integrated luminosity, lepton reconstruction and nonprompt background have the greatest effect both on the $t\bar{t}W$ and $t\bar{t}Z$ cross-section measurement. In addition to these the uncertainty on WZ background gives a significant contribution to the systematic uncertainty of $t\bar{t}Z$ cross section measurement. The full set of systematic uncertainties is shown in Table 1.

Table 1: Summary of the sources of uncertainties, their magnitudes and effects. The first column shows the input uncertainty on each background and signal, while the second and third columns are the postfit uncertainties on $t\bar{t}W$ and $t\bar{t}Z$ cross-section measurements respectively.

Source	Uncertainty range	Impact on ttW cross-section	Impact on ttZ cross-section
Luminosity	2.5%	4%	3%
Jet Energy Scale/Resolution	2-5%	3%	3%
Trigger	2-4%	4-5%	5%
B tagging	1-5%	2-5%	4-5%
PU modeling	1%	1%	1%
Lepton ID, efficiency	2-7%	3%	6-7%
μ_R/μ_F scale choice	1%	<1%	1%
PDF choice	1%	<1%	1%
Nonprompt background	30%	4%	$<2\%$
WZ cross section	10-20%	<1%	2%
ZZ cross section	20%	-	1%
Charge misidentification	20%	3%	-
Rare SM background	50%	2%	2%
ttX background	10-15%	4%	3%
Stat. unc. for nonprompt	5-50%	4%	2%
Stat. unc. rare SM processes	20-100%	1%	$<1\%$
Total systematic	-	14%	12%

6 Results

As described in section 3 the data events are analyzed in three exclusive channels according to the number of leptons in the final state: same-charge dilepton, three and four lepton. In each channel events are further categorized according to the number of jets and b tagged jets. Predicted SM backgrounds, the signal yields and the observed data events are shown in Figs. 10-12 and Tables 2-10 for each category in same-charge dilepton, three and four lepton channels respectively. We find in general good agreement between the predicted yields and the observed data except a slight excess of events accumulated in N_{jets} =2,3 $N_{\text{b jets}} \geq 2$ category of three lepton channel (see 7th and 8th bins in Fig. 11). Extensive studies are performed to ensure the robustness of the estimated background yields in this region. No hits of missing or underestimation of backgrounds was found, thus we attribute this to a statistical fluctuation in data. In Figs. 8 and 9 various kinematic distributions of predicted and observed yields are presented in

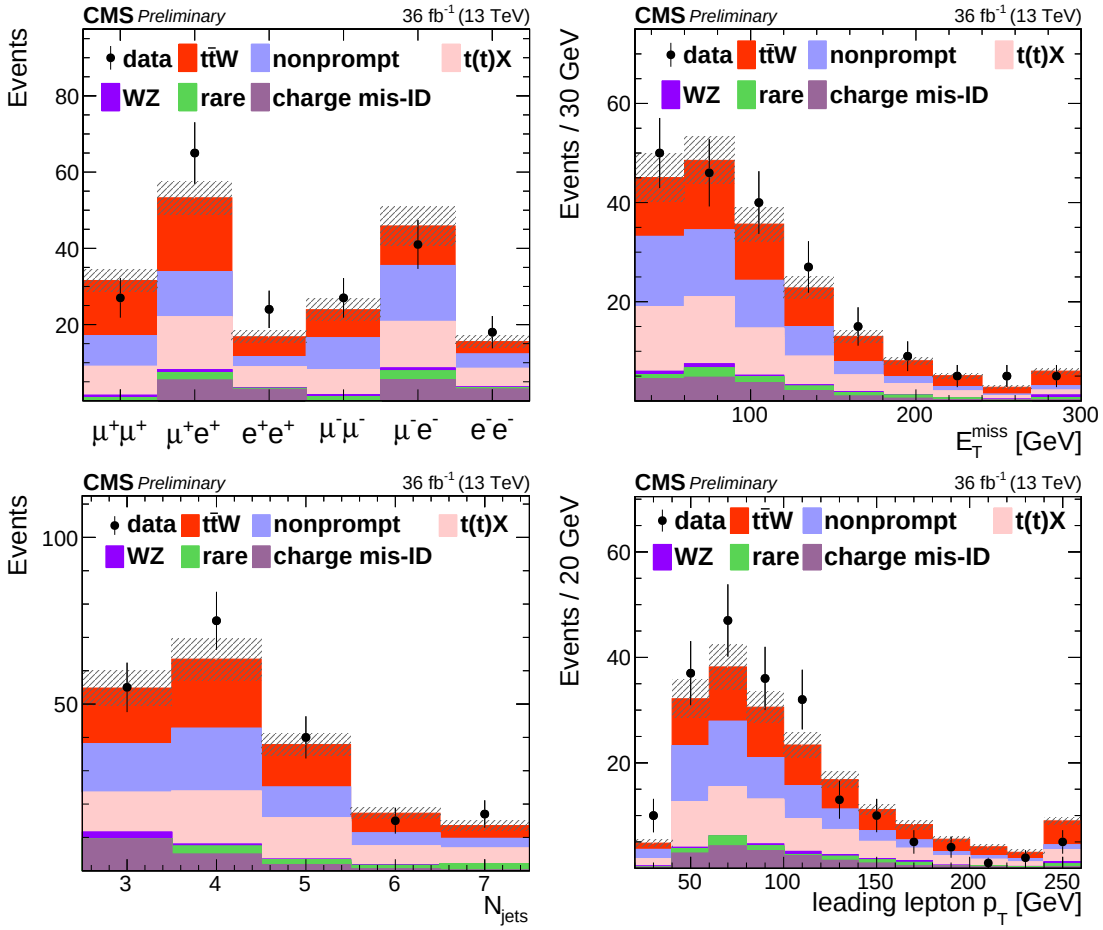

Figure 8: Distributions of the predicted and observed yields versus the kinematic variables in $t\bar{t}W$ signal enriched region for same charge dilepton channel.

$t\bar{t}W$ and $t\bar{t}Z$ signal enriched regions: same-charge dileptons with $N_{\text{jets}} \geq 3$ and $N_{\text{b jets}} \geq 2$ and three lepton events with $N_{\text{jets}} \geq 3$ and $N_{\text{b jets}} \geq 1$, respectively.

The statistical procedure to extract the cross section is described in detail in [35]. The observed yields and background estimates in Tables 2-10 and the systematic uncertainties described in Sec. 5 are used to construct a binned likelihood function $L(r, \theta)$ as a product of Poisson probabilities from all bins. The parameter r is the signal strength modifier and θ represents the full suite of nuisance parameters. The signal strength parameter $r = 1$ corresponds to a signal cross section equal to the SM prediction, while $r = 0$ corresponds to the background-only hypothesis.

The profile likelihood ratio test statistic $q(r) = -2L(r, \hat{\theta}_r)/L(\hat{r}, \hat{\theta})$ is used to extract the asymptotic best-fit cross section, the associated uncertainties and the significance of the observation of the signal process [36]. Here, $\hat{\theta}_r$ are the values for nuisance parameters which maximize the likelihood function for signal strength r. The quantities $\hat{r}$ and $\hat{\theta}$ are the values that simultaneously maximise L.

We find an expected signal significance of 4.6 standard deviations in the same-sign two-lepton channel from the background-only hypothesis and 8.4 and 4.7 standard deviations in the three- and four-lepton channels, respectively. The observed significances are 5.5, 8.7 and 4.6 respectively. The combined significance of the 3- and 4-lepton channels together is 9.5 (expected) and 9.9 (observed), as shown in Table 11.

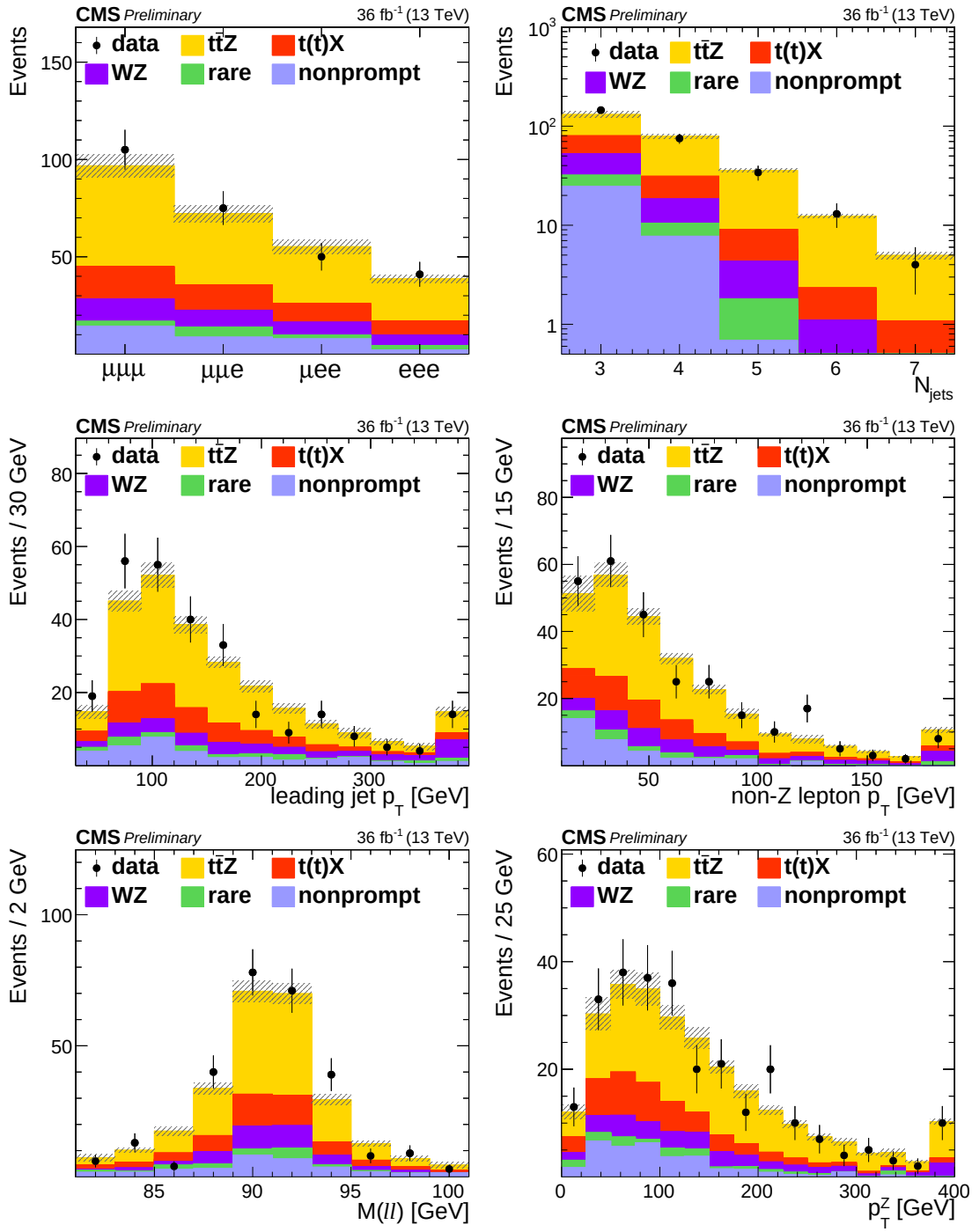

Figure 9: Distributions of the predicted and observed yields versus the kinematic variables in $t\bar{t}Z$ signal enriched region for three lepton channel.

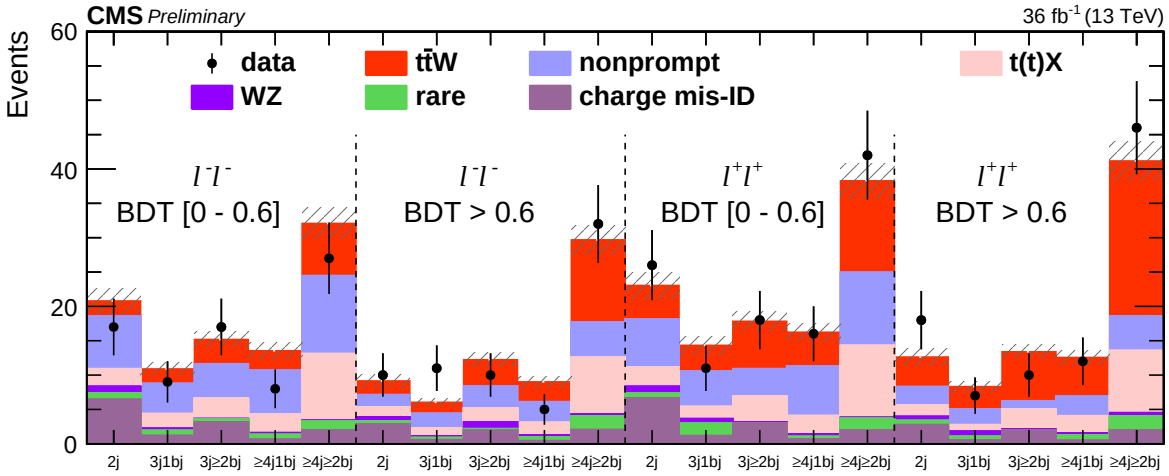

Figure 10: Post-fit predicted and observed yields in each analysis bin in the same-sign dilepton analysis.The hatched band shows the total uncertainty associated to signal and background predictions.

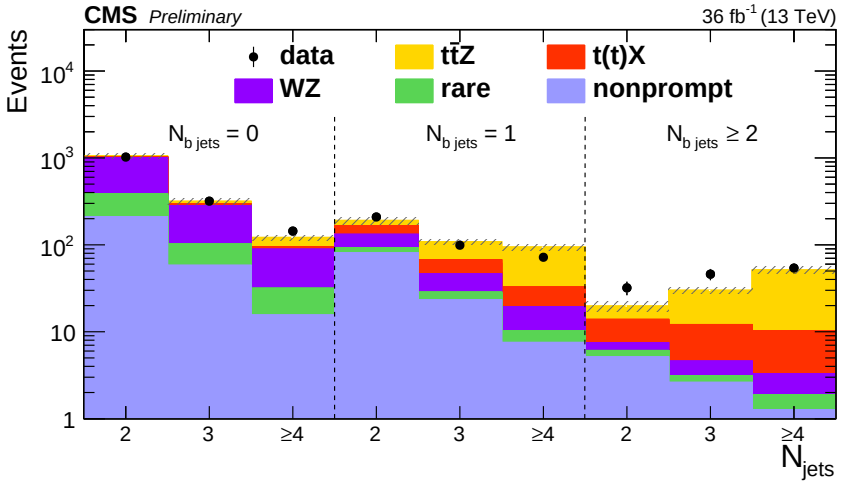

Figure 11: Post-fit predicted and observed yields in $N_{\text{jets}} = 2, 3$ and ≥ 4 categories in the three-lepton analyses. The hatched band shows the total uncertainty associated to signal and background predictions.

	2 leptons $\ell^{\pm}\ell^{\pm}$, BDT < 0		
Process	$N_{\text{jets}} = 2$	$N_{\text{jets}} = 3$	$N_{\text{jets}} \geq 4$
nonprompt	136.52 ± 13.94	110.32 ± 11.33	57.30 ± 6.07
Total background	193.62 ± 15.34	140.70 ± 11.74	78.00 ± 6.48
$t\bar{t}W$	13.11 ± 1.34	17.55 ± 1.78	13.80 ± 1.42
Total	206.74 ± 15.40	158.26 ± 11.87	91.80 ± 6.63
Observed	229	144	92

Table 2: Post-fit predicted and observed yields in same-sign dilepton final state for BDT < 0 region, i.e. nonprompt control region. The uncertainty represents the total post-fit uncertainty.

The measured signal strength parameter is found to be $1.28\ ^{+0.19}_{-0.18}(\text{stat.})\ ^{+0.20}_{-0.18}(\text{sys.})\ ^{+0.13}_{-0.12}(\text{theo.})$ for $t\bar{t}W$ and $1.18\ ^{+0.11}_{-0.10}(\text{stat.})\ ^{+0.14}_{-0.12}(\text{sys})\ ^{+0.11}_{-0.12}(\text{theo.})$ for $t\bar{t}Z$. This value is multiplied by the corre-

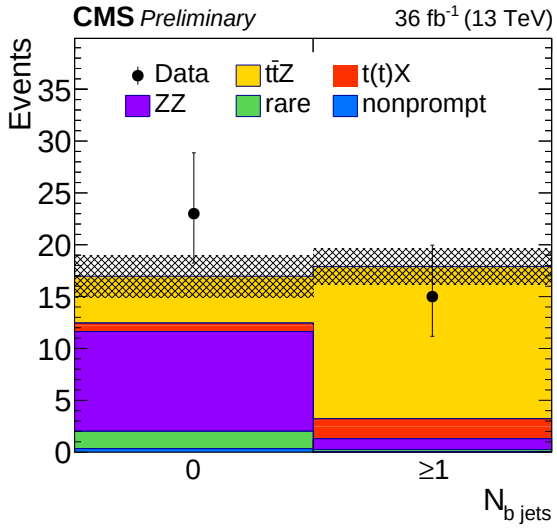

Figure 12: Post-fit predicted and observed yields in the four-lepton analyses. The hatched band shows the total uncertainty associated to signal and background predictions.

	2 leptons $\ell^-\ell^-$, $0 <$ BDT < 0.6				
Process	$N_{\text{jets}} = 2$	$N_{\text{jets}} = 3$		$N_{\text{jets}} \geq 4$	
	$N_{\text{b jets}} \geq 1$	$N_{\text{b jets}} = 1$	$N_{\text{b jets}} \geq 2$	$N_{\text{b jets}} = 1$	$N_{\text{b jets}} \geq 2$
Total background	18.60 ± 1.82	8.78 ± 0.88	11.65 ± 1.13	10.71 ± 1.17	24.47 ± 2.10
$t\bar{t}W$	2.19 ± 0.25	2.11 ± 0.24	3.53 ± 0.38	2.83 ± 0.32	7.60 ± 0.80
Total	20.79 ± 1.84	10.89 ± 0.91	15.18 ± 1.19	13.54 ± 1.21	32.07 ± 2.25
Observed	17	9	17	8	27

Table 3: Post-fit predicted and observed yields in same-sign dilepton final state for $0 <$ BDT < 0.6 region where the sign of both leptons are negative. The uncertainty represents the total post-fit uncertainty.

	2 leptons $\ell^-\ell^-$, BDT > 0.6				
Process	$N_{\text{jets}} = 2$	$N_{\text{jets}} = 3$		$N_{\text{jets}} \geq 4$	
	$N_{\text{b jets}} \geq 1$	$N_{\text{b jets}} = 1$	$N_{\text{b jets}} \geq 2$	$N_{\text{b jets}} = 1$	$N_{\text{b jets}} \geq 2$
Total background	7.15 ± 0.88	4.43 ± 0.57	8.40 ± 0.89	6.12 ± 0.73	17.73 ± 1.67
$t\bar{t}W$	2.00 ± 0.22	1.61 ± 0.19	3.84 ± 0.41	2.89 ± 0.33	11.96 ± 1.23
Total	9.15 ± 0.91	6.03 ± 0.60	12.24 ± 0.98	9.01 ± 0.80	29.68 ± 2.07
Observed	10	11	10	5	32

Table 4: Post-fit predicted and observed yields in same-sign dilepton final state for BDT > 0.6 region where the sign of both leptons are negative. The uncertainty represents the total post-fit uncertainty.

sponding theoretical cross sections for $t\bar{t}W$ and $t\bar{t}Z$, mentioned in Sec. 1, to obtain the measured cross section of $t\bar{t}W$ and $t\bar{t}Z$:

$$\sigma(pp \to t\bar{t}Z) = 1.00^{+0.09}_{-0.08}(\text{stat.})\ ^{+0.12}_{-0.10}(\text{sys.})\ \text{pb}$$

Process	2 leptons $\ell^+\ell^+$, $0 <$ BDT < 0.6				
	$N_{\text{jets}} = 2$	$N_{\text{jets}} = 3$		$N_{\text{jets}} \geq 4$	
	$N_{\text{b jets}} \geq 1$	$N_{\text{b jets}} = 1$	$N_{\text{b jets}} \geq 2$	$N_{\text{b jets}} = 1$	$N_{\text{b jets}} \geq 2$
Total background	18.13 ± 1.84	10.58 ± 1.27	10.93 ± 1.18	11.34 ± 1.19	24.96 ± 2.13
$t\bar{t}W$	4.91 ± 0.52	3.74 ± 0.40	6.90 ± 0.72	4.90 ± 0.53	13.31 ± 1.37
Total	23.04 ± 1.91	14.33 ± 1.33	17.83 ± 1.38	16.23 ± 1.30	38.27 ± 2.53
Observed	26	11	18	16	42

Table 5: Post-fit predicted and observed yields in same-sign dilepton final state for $0 <$ BDT < 0.6 region where the sign of both leptons are positive. The uncertainty represents the total post-fit uncertainty.

Process	2 leptons $\ell^+\ell^+$, BDT > 0.6				
	$N_{\text{jets}} = 2$	$N_{\text{jets}} = 3$		$N_{\text{jets}} \geq 4$	
	$N_{\text{b jets}} \geq 1$	$N_{\text{b jets}} = 1$	$N_{\text{b jets}} \geq 2$	$N_{\text{b jets}} = 1$	$N_{\text{b jets}} \geq 2$
Total background	8.32 ± 1.08	5.09 ± 0.73	6.26 ± 0.71	6.93 ± 0.84	18.63 ± 1.68
$t\bar{t}W$	4.31 ± 0.46	3.23 ± 0.35	7.13 ± 0.74	5.63 ± 0.60	22.54 ± 2.29
Total	12.63 ± 1.17	8.32 ± 0.81	13.39 ± 1.03	12.56 ± 1.04	41.16 ± 2.84
Observed	18	7	10	12	46

Table 6: Post-fit predicted and observed yields in same-sign dilepton final state for BDT > 0.6 region where the sign of both leptons are positive. The uncertainty represents the total post-fit uncertainty.

Process	3-leptons, $N_{\text{b jets}} = 0$		
	$N_{\text{jets}} = 2$	$N_{\text{jets}} = 3$	$N_{\text{jets}} \geq 4$
Total background	1033.76 ± 77.15	294.09 ± 21.43	95.44 ± 7.41
$t\bar{t}Z$	18.21 ± 1.85	22.33 ± 2.26	26.12 ± 2.65
Total	1051.97 ± 77.17	316.41 ± 21.55	121.56 ± 7.87
Observed	1022	318	144

Table 7: Post-fit predicted and observed yields in three-lepton final state in $N_{\text{b jets}} = 0$ category. The uncertainty represents the total post-fit uncertainty.

Process	3-leptons, $N_{\text{b jets}} = 1$		
	$N_{\text{jets}} = 2$	$N_{\text{jets}} = 3$	$N_{\text{jets}} \geq 4$
Total background	166.48 ± 17.79	67.18 ± 6.66	32.72 ± 3.32
$t\bar{t}Z$	24.27 ± 2.44	41.19 ± 4.13	61.31 ± 6.17
Total	190.75 ± 17.95	108.37 ± 7.84	94.04 ± 7.00
Observed	209	99	72

Table 8: Post-fit predicted and observed yields in three-lepton final state in $N_{\text{b jets}} = 1$ category. The uncertainty represents the total post-fit uncertainty.

$$\sigma(\text{pp} \to t\bar{t}W) = 0.80\ ^{+0.12}_{-0.11}(\text{stat.})\ ^{+0.13}_{-0.12}(\text{sys.})\ \text{pb}$$

The expected(observed) signal significances for $t\bar{t}W^+$ and $t\bar{t}W^-$ processes are calculated as well,

	3-leptons, $N_{\text{b jets}} \geq 2$		
Process	$N_{\text{jets}} = 2$	$N_{\text{jets}} = 3$	$N_{\text{jets}} \geq 4$
Total background	13.88 ± 2.39	12.10 ± 1.74	10.25 ± 1.60
$t\bar{t}Z$	5.86 ± 0.60	17.88 ± 1.81	41.01 ± 4.13
Total	19.74 ± 2.47	29.98 ± 2.51	51.27 ± 4.43
Observed	32	46	54

Table 9: Post-fit predicted and observed yields in three-lepton final state in $N_{\text{b jets}} \geq 2$ category. The uncertainty represents the total post-fit uncertainty.

	4-leptons, $N_{\text{jets}} \geq 2$	
Process	$N_{\text{b jets}} = 0$	$N_{\text{b jets}} \geq 1$
Total background	12.45 ± 1.92	3.22 ± 0.29
$t\bar{t}Z$	4.52 ± 0.58	14.69 ± 1.74
Total	16.97 ± 2.00	17.91 ± 1.76
Observed	23	15

Table 10: Post-fit predicted and observed yields in four-lepton final state. The uncertainty represents the total post-fit uncertainty.

4.2 (5.5) and 2.4(2.3) respectively. The cross section for the $t\bar{t}W^+$ and $t\bar{t}W^-$ processes are the following:

$$\sigma(pp \to t\bar{t}W^+) = 0.58\ ^{+0.09}_{-0.09}(\text{stat.})\ ^{+0.09}_{-0.08}(\text{sys.})\ \text{pb},$$

$$\sigma(pp \to t\bar{t}W^-) = 0.19\ ^{+0.07}_{-0.07}(\text{stat.})\ ^{+0.06}_{-0.06}(\text{sys.})\ \text{pb}.$$

The results of the individual fits are summarized in Fig. 13 as well as a simultaneous fit of the cross sections of the two processes using all dilepton, three-lepton, and four-lepton channels. The cross section extracted from this two-dimensional fit for $t\bar{t}Z$ is identical to that obtained from the two one-dimensional fit, while for $t\bar{t}W$ the two-dimensional fit is shifted down by $\approx 3\%$ towards the theoretical prediction. This is because the best-fit value for the nonprompt contribution in the three-lepton channel is 12% higher than the nominal value, so the best-fit nonprompt yields in the same-sign dilepton channel are higher in the combined fit than in the individual fit.

7 Effective field theory interpretation

Under effective field theory, cross section measurements can be used to search in a model-independent way for new physics (NP) at energy scales which are not yet experimentally accessible. Using this approach, the SM Lagrangian is extended with higher-order operators which correspond to combinations of SM fields. The extended Lagrangian is a series expansion in the inverse of the energy scale of the new physics, $1/\Lambda$ [37], hence operators are supressed as long as Λ is large compared with the experimentally-accessible energy.

Channel	Expected significance	Observed significance
$2\ell ss$ analysis $t\bar{t}W^-$	2.4	2.3
$2\ell ss$ analysis $t\bar{t}W^+$	4.3	5.9
$2\ell ss$ analysis ($t\bar{t}W$)	4.6	5.5
3ℓ analysis ($t\bar{t}Z$)	8.4	8.7
4ℓ analysis ($t\bar{t}Z$)	4.8	4.6
3ℓ and 4ℓ combined ($t\bar{t}Z$)	9.5	9.9

Table 11: Summary of expected and observed significance for $t\bar{t}W$ in the same-sign 2-lepton channel and for $t\bar{t}Z$ in the 3-lepton, 4-lepton channels and in the two channels combined.

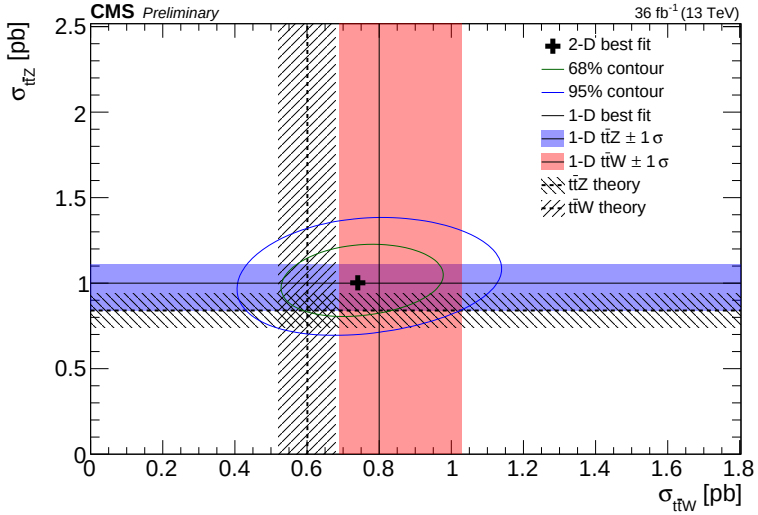

Figure 13: The result of the two-dimensional best fit for $t\bar{t}W$ and $t\bar{t}Z$ cross sections (cross symbol) is shown along with its 68 and 95% confidence level contours. The result of this fit is superimposed with the separate $t\bar{t}W$ and $t\bar{t}Z$ cross section measurements, and the corresponding 1 σ bands, obtained from the dilepton, and the three-lepton/four-lepton channels, respectively. The figure also shows the predictions from theory and the corresponding uncertainties.

The effective Lagrangian is:

$$\mathcal{L}_{\text{eff}} = \mathcal{L}_{\text{SM}} + \frac{1}{\Lambda}\sum_i c_i \mathcal{O}_i + \frac{1}{\Lambda^2}\sum_j c_j \mathcal{O}_j + \cdots \tag{4}$$

where $\mathcal{L}_{\text{SM}}$ is the dimension-four SM Lagrangian, $\mathcal{O}_i$ are dimension-five operators, $\mathcal{O}_j$ are dimension-six operators, etc. The Wilson coefficients c_i and c_j parameterize the strength of the NP interaction.

Because dimension-five operators violate lepton number conservation [37], we do not consider them in our investigation. Assuming baryon and lepton number conservation, there are fifty-nine independent dimension-six operators [38]. Thirty-nine of these operators include at least one Higgs field, or may be important for Higgs physics because they modify the gauge boson self-interactions [39]. Constraints on some dimension-six operators have been reported in [5, 40–46].

To investigate the effects of NP on a given process, it is necessary to calculate the expected cross section as a function of the Wilson coefficients. The matrix element can be written as the sum of an SM and NP components:

$$\mathcal{M} = \mathcal{M}_0 + \sum c_j \mathcal{M}_j \tag{5}$$

In this work, we consider one operator at a time:

$$\mathcal{M} = \mathcal{M}_0 + c_1 \mathcal{M}_1 \tag{6}$$

The cross section is proportional to the matrix element squared, and has the following structure [43]:

$$\sigma(c_1) \propto |\mathcal{M}|^2 \tag{7}$$
$$\propto s_0 + s_1 c_1 + s_2 c_1^2 \tag{8}$$

Note from the above relation that while $\sigma(c_1)$ is always quadratic, the minimum is not constrained to appear at the SM value ($c_1 = 0$), and in cases where an operator interferes destructively with the SM it is possible to have $\sigma_{\text{SM+NP}}(c_j) < \sigma_{\text{SM}}$.

The dimension-six operators were encoded using the the FeynRules [47] implementation from [39], and will follow their notation and operator naming scheme throughout this work. This implementation assumes flavour-independent fermion couplings. Because the W and Z couplings to light quarks are highly constrained by other measurements, we removed all NP couplings to the first two generations. This modified implementation was used with MG5_AMC@NLO [9] to evaluate the cross section $\sigma_{\text{SM+NP}}$ expected due to both SM and NP effects at leading order for 30 values of c_j in the range $[-1, 1]$ (with all other couplings set to their SM values). We then fit those points with a quadratic function (see Eq. 7) to determine $\sigma_{\text{SM+NP}}(c_j)$.

Because it is an irreducible background to $t\bar{t}W$, we considered NP effects on $t\bar{t}H$ as well as $t\bar{t}W$ and $t\bar{t}Z$. The signal strength $r_{t\bar{t}Z}(c_j)$ was defined as the ratio of $\sigma_{\text{SM+NP},t\bar{t}Z}(c_j)$ to $\sigma_{\text{SM+NP},t\bar{t}Z}(0)$ and similarly for $t\bar{t}W$ and $t\bar{t}H$. From this we construct a profile likelihood test statistic $q(c_j)$. The likelihood statistic was maximized to find the asymptotic best-fit c_j, similarly to what is described in Section 6. Each coupling is profiled with the other couplings set to their SM values.

The expected 2σ CL interval was calculated for the thirty-nine Wilson coefficients included in [39]. We excluded operators for which this interval contained any $|c_j| > 10$, as the effective field theory expansion breaks down for large c_j. We also excluded operators which caused the cross section to be scaled by more than 1.3 for $t\bar{t}$, inclusive Higgs, WW, or WZ, and operators which produced a significant effect on background yields, as these could be better studied in other signal regions.

Four operators were found to satisfy all of these requirements, and constraints on their Wilson coefficients, $\bar{c}_{uW}$, $\bar{c}_{uB}$, $\bar{c}_u$, and $\bar{c}_{Hu}$ are reported here. Example Feynman diagrams for these operators are shown in Fig. 14. The calculated signal strengths $r(c_j)$ are shown in Fig. 15 for $t\bar{t}Z$, $t\bar{t}W$, and $t\bar{t}H$. The operators proportional to $\bar{c}_{uW}$ and $\bar{c}_{uB}$ affect multiple processes and do not produce destructive interference with the SM. The operators proportional to $\bar{c}_u$ and $\bar{c}_{Hu}$ only have a significant affect on one of the examined processes each ($t\bar{t}H$ and $t\bar{t}Z$ respectively) and produce destructive interference with the SM.

The expected CL intervals for the selected Wilson coefficients are summarized in Table 12. Observed best fit values and CL intervals for the selected Wilson coefficients are presented in

Fig. 16 and summarized in Table 13. We removed any assumptions about the energy scale of the NP made in [39] and report the ratio c_j/Λ^2. Due to the quadratic dependency of the cross section on Wilson coefficients (see Eq. 7), except where $\sigma_{\mathrm{SM+NP}}(c_j)$ is minimized, there will always be two values of c_j corresponding to the same cross section. This can result in multiple minima in the profile likelihood scans, as seen in Fig. 16. When the Wilson coefficient affects more than one process, and the minima in the corresponding $\sigma_{\mathrm{SM+NP}}(c_j)$ do not coincide, the symmetry is broken and there should be one optimal best fit value. For $\bar{c}_u$ and $\bar{c}_{uB}$, there was no significant difference between the two best fit values, so we show the degeneracy explicitly by transforming such that the axis of symmetry is at the origin.

In Fig. 17, results are shown in the $\sigma_{\mathrm{t\bar{t}Z}}$ versus $\sigma_{\mathrm{t\bar{t}W}}$ plane. The 1σ (2σ) contours are obtained by sampling randomly from the post-fit covariance matrix and finding the contour which encloses 68.27% (95.45%) of the samples. The operators proportional to $\bar{c}_u$, $\bar{c}_{uB}$, and $\bar{c}_{Hu}$ all affect $\mathrm{t\bar{t}Z}$ and the fit is able to scale $\mathrm{t\bar{t}Z}$ to match the observed excess in data. The $\bar{c}_u$ coefficient does not affect $\mathrm{t\bar{t}Z}$ or $\mathrm{t\bar{t}W}$, but the fit can scale $\mathrm{t\bar{t}H}$ to accomodate the $\mathrm{t\bar{t}W}$ excess. The only coefficient which affects $\mathrm{t\bar{t}W}$ is $\bar{c}_{uW}$, but it also affects $\mathrm{t\bar{t}H}$. In this case both $\mathrm{t\bar{t}H}$ and $\mathrm{t\bar{t}W}$ are scaled.

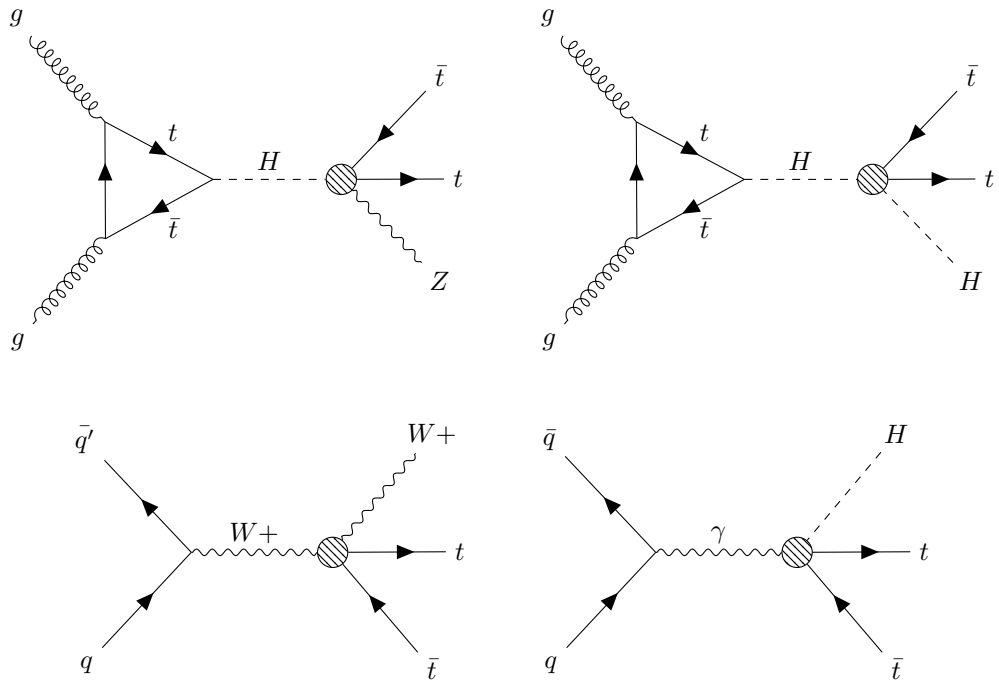

Figure 14: Example Feynman diagrams involving NP vertices due to the operator which is proportional to $\bar{c}_{Hu}$ (top left), $\bar{c}_u$ (top right), $\bar{c}_{uW}$ (bottom left), and $\bar{c}_{uB}$ (bottom right). These NP vertices do not appear in the SM.

Wilson coefficient	1σ CL $[\mathrm{TeV}^{-2}]$	2σ CL $[\mathrm{TeV}^{-2}]$
$\lvert\bar{c}_{uB}/\Lambda^2 + 0.1\,\mathrm{TeV}^{-2}\rvert$	[0.0, 2.9]	[0.0, 4.1]
$\lvert\bar{c}_u/\Lambda^2 + 18.5\,\mathrm{TeV}^{-2}\rvert$	[3.9, 25.8]	[0.0, 31.7]
$\bar{c}_{uW}/\Lambda^2$	[-1.9, 1.8]	[-3.5, 3.2]
$\bar{c}_{Hu}/\Lambda^2$	[-9.1, -6.5] and [-1.6, 1.1]	[-10.0, 2.0]

Table 12: Expected 1σ and 2σ CL for this $\mathrm{t\bar{t}W}$ and $\mathrm{t\bar{t}Z}$ measurement, for selected Wilson coefficients.

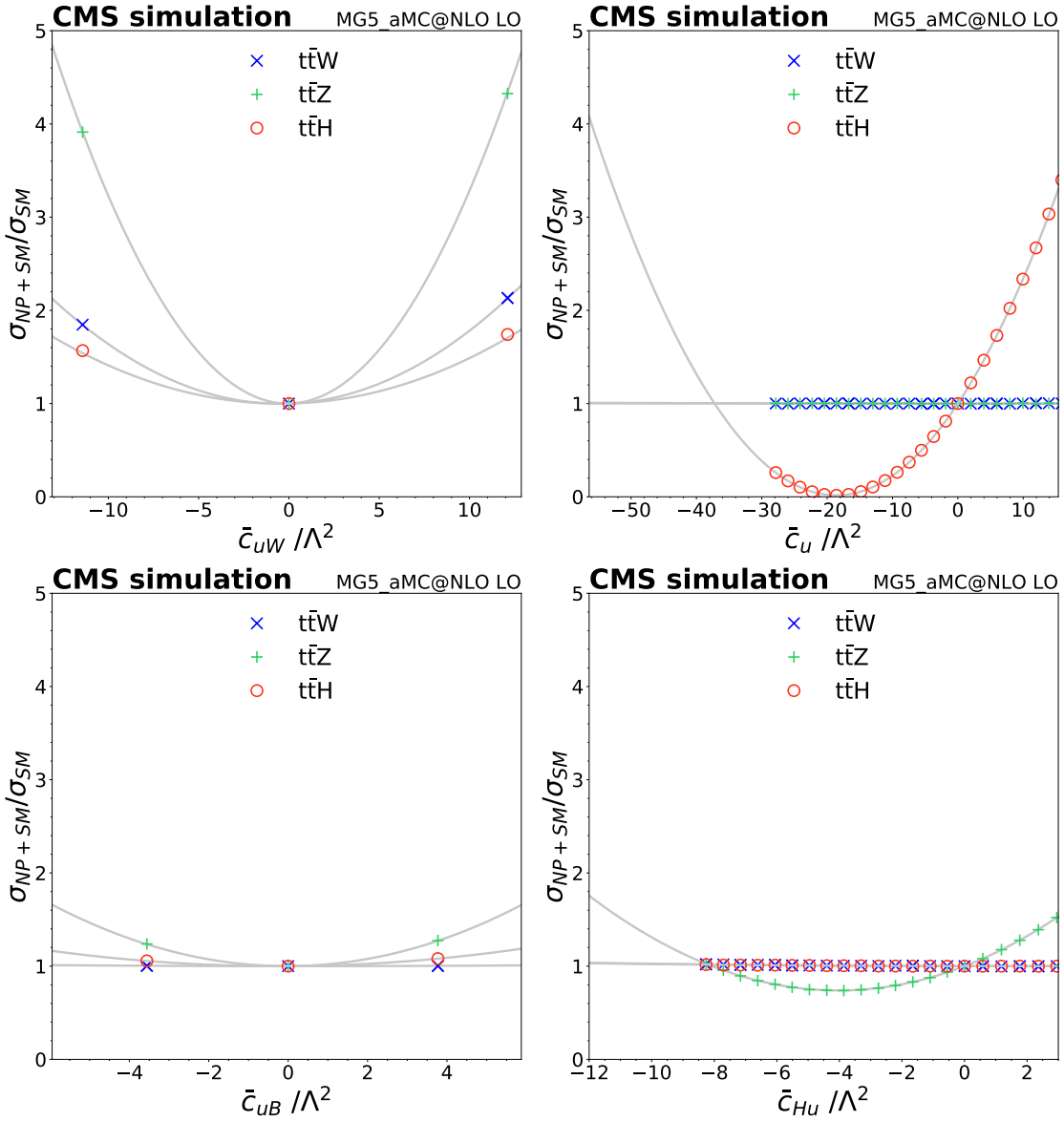

Figure 15: Signal strength as a function of c_j for $\bar{c}_{uW}$ (top left), $\bar{c}_u$ (top right), $\bar{c}_{uB}$ (bottom left), and $\bar{c}_{Hu}$ (bottom right). All three processes are affected by $\bar{c}_{uW}$, while only $t\bar{t}H$ is affected by $\bar{c}_u$ and only $t\bar{t}Z$ is affected by $\bar{c}_{Hu}$. Both $t\bar{t}Z$ and $t\bar{t}H$ sensitive to $\bar{c}_{uB}$.

Wilson coefficient	Best fit $[\mathrm{TeV}^{-2}]$	1σ CL $[\mathrm{TeV}^{-2}]$	2σ CL $[\mathrm{TeV}^{-2}]$
$\lvert\bar{c}_{uB}/\Lambda^2 + 0.1\,\mathrm{TeV}^{-2}\rvert$	3.2	[0.0, 4.4]	[0.0, 5.4]
$\lvert\bar{c}_{u}/\Lambda^2 + 18.5\,\mathrm{TeV}^{-2}\rvert$	19.1	[5.0, 26.4]	[0.0, 32.5]
$\bar{c}_{uW}/\Lambda^2$	3.0	[-4.1, -1.5] and [1.2, 4.1]	[-5.1, 5.0]
$\bar{c}_{Hu}/\Lambda^2$	-9.4	[-10.3, -8.1] and [0.1, 2.1]	[-11.1, -6.6] and [-1.4, 3.0]

Table 13: Observed best-fit values determined from this $t\bar{t}W$ and $t\bar{t}Z$ measurement, along with corresponding 1σ and 2σ CL intervals for selected Wilson coefficients.

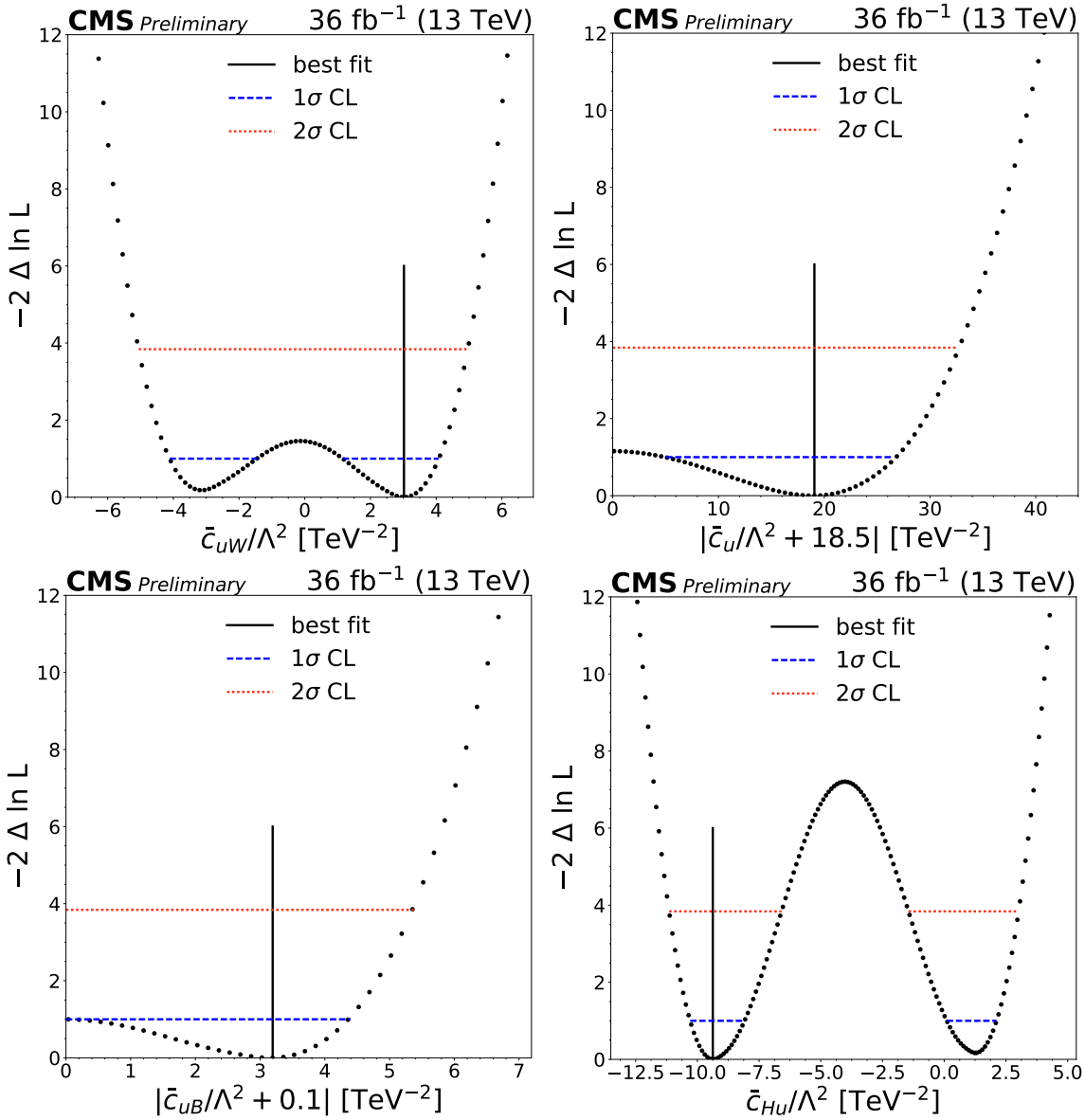

Figure 16: The 1D test statistic $q(c_j)$ scan versus c_j, profiling all other nuisance parameters, for $\bar{c}_{uW}$ (top left), $\bar{c}_u$ (top right), $\bar{c}_{uB}$ (bottom left), and $\bar{c}_{Hu}$ (bottom right). The best-fit value is indicated by a solid line. Dotted lines and dashed lines indicate 1 σ CLs and 2 σ CLs, respectively.

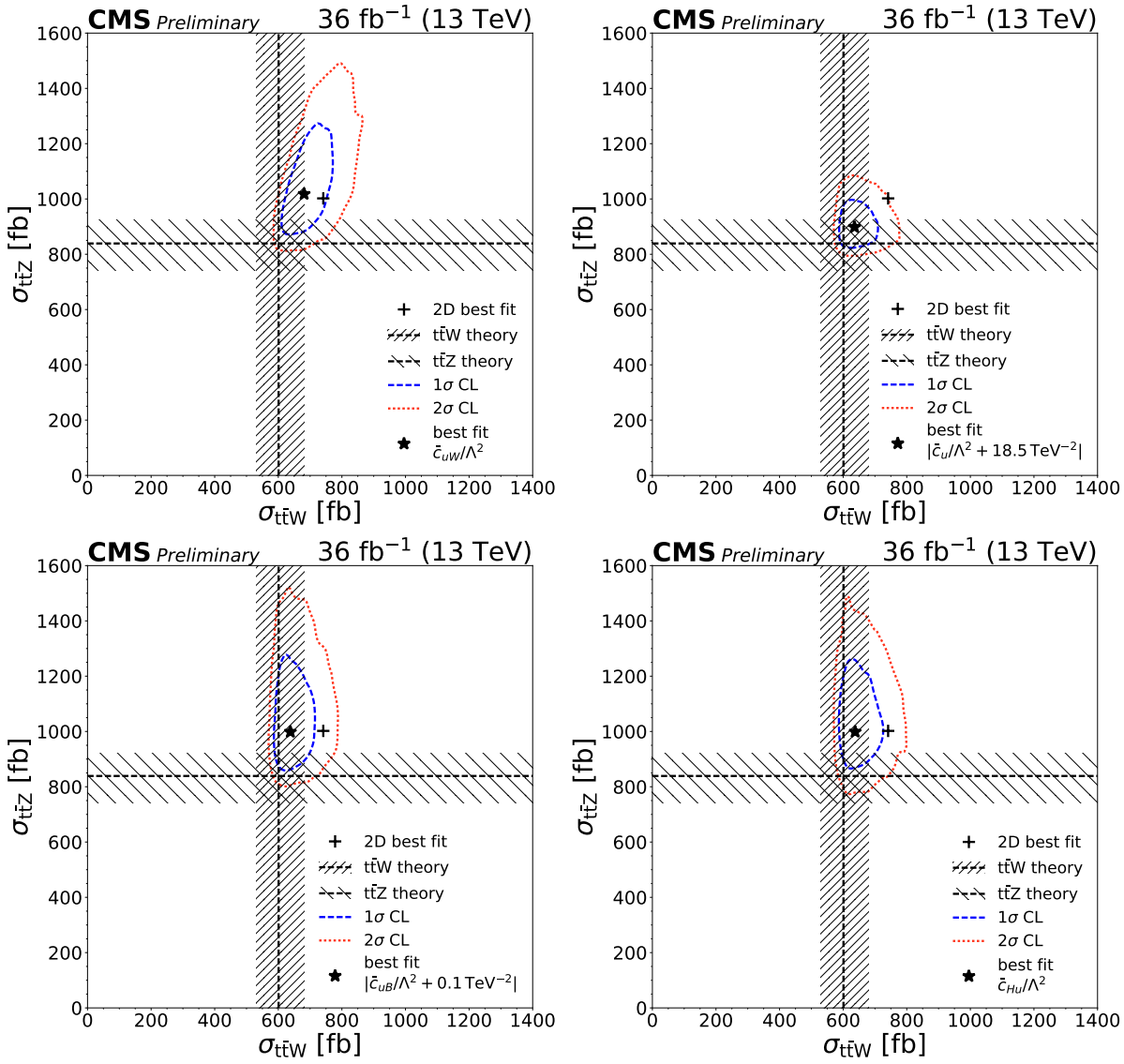

Figure 17: The $t\bar{t}Z$ and $t\bar{t}W$ cross section corresponding to the best-fit value of $\bar{c}_{uW}$ (top left), $\bar{c}_u$ (top right), $\bar{c}_{uB}$ (bottom left), and $\bar{c}_{Hu}$ (bottom right) is shown as a star, along with the corresponding 1σ (red) and 2σ (blue) contours. The two-dimensional best fit to the $t\bar{t}W$ and $t\bar{t}Z$ cross sections is shown as a cross symbol. Predictions from theory at NLO (dotted lines) and their uncertanties (hatches) are also shown.

8 Conclusions

A measurement of top quark pair production in association with a W or a Z boson using 13 TeV data is presented. The analysis is performed in the same-sign dilepton final state for $t\bar{t}W$ and the three- and four-lepton final states for $t\bar{t}Z$, and these three are used to extract the cross sections of $t\bar{t}W$ and $t\bar{t}Z$ production. The same-sign dilepton channel achieves a significance of 5.5 standard deviations, the three-lepton analysis 8.7 standard deviations and the four-lepton analysis 4.6 standard deviatations. From the combination of three- and four-lepton channels a significance of 9.9 standard deviations for $t\bar{t}Z$ is obtained. The measured cross sections are $\sigma(t\bar{t}Z) = 1.00^{+0.09}_{-0.08}(\text{stat.})\ ^{+0.12}_{-0.10}(\text{sys.})$ pb and $\sigma(t\bar{t}W) = 0.80\ ^{+0.12}_{-0.11}(\text{stat.})\ ^{+0.13}_{-0.12}(\text{sys.})$ pb, in agreement with the standard model predictions. These results have been used to set constraints on the Wilson coefficients of four operators which would modify $t\bar{t}Z$ and $t\bar{t}W$ production.

References

[1] B. Mellado Garcia, P. Musella, M. Grazzini, and R. Harlander, "CERN Report 4: Part I Standard Model Predictions", Technical Report LHCHXSWG-DRAFT-INT-2016-008, 2016.

[2] CMS Collaboration, "The CMS experiment at the CERN LHC", *JINST* **3** (2008) S08004, doi:10.1088/1748-0221/3/08/S08004.

[3] CMS Collaboration, "Measurement of associated production of vector bosons and $t\bar{t}$ in pp collisions at $\sqrt{s} = 7$ TeV", *Phys. Rev. Lett.* **110** (2013) 172002, doi:10.1103/PhysRevLett.110.172002, arXiv:1303.3239.

[4] CMS Collaboration, "Measurement of top quark-antiquark pair production in association with a W or Z boson in pp collisions at $\sqrt{s} = 8$ TeV", *Eur. Phys. J.C* **74** (2014), no. 9, 3060, doi:10.1140/epjc/s10052-014-3060-7, arXiv:1406.7830.

[5] CMS Collaboration, "Observation of top quark pairs produced in association with a vector boson in pp collisions at $\sqrt{s} = 8$ TeV", *JHEP* **01** (2016) 096, doi:10.1007/JHEP01(2016)096, arXiv:1510.01131.

[6] ATLAS Collaboration, "Measurement of the $t\bar{t}W$ and $t\bar{t}Z$ production cross sections in pp collisions at $\sqrt{s} = 8$ TeV with the ATLAS detector", *JHEP* **11** (2015) 172, doi:10.1007/JHEP11(2015)172, arXiv:1509.05276.

[7] ATLAS Collaboration, "Measurement of the $t\bar{t}Z$ and $t\bar{t}W$ production cross sections in multilepton final states using 3.2 fb^{-1} of pp collisions at $\sqrt{s} = 13$ TeV with the ATLAS detector", *Eur. Phys. J. C.* doi:10.1140/epjc/s10052-016-4574-y, arXiv:1609.01599.

[8] J. Alwall et al., "MADGRAPH 5 : Going Beyond", *JHEP* **06** (2011) 128, doi:10.1007/JHEP06(2011)128, arXiv:1106.0522.

[9] S. Frixione and B. R. Webber, "Matching NLO QCD computations and parton shower simulations", *JHEP* **06** (2002) 29, arXiv:hep-ph/0204244.

[10] T. Sjöstrand, S. Mrenna, and P. Skands, "PYTHIA 6.4 physics and manual", *JHEP* **05** (2006) 026, doi:10.1088/1126-6708/2006/05/026, arXiv:hep-ph/0603175.

[11] T. Sjostrand et al., "An Introduction to PYTHIA 8.2", *Comput. Phys. Commun.* **191** (2015) 159–177, doi:10.1016/j.cpc.2015.01.024, arXiv:1410.3012.

[12] S. Alioli et al., "NLO single-top production matched with shower in POWHEG: s- and t-channel contributions", *JHEP* **09** (2009) 111, doi:10.1088/1126-6708/2009/09/111, arXiv:0907.4076.

[13] S. Alioli et al., "A general framework for implementing NLO calculations in shower Monte Carlo programs: the POWHEG BOX", *JHEP* **06** (2010) 043, doi:10.1007/JHEP06(2010)043, arXiv:1002.2581.

[14] J. M. Campbell and R. K. Ellis, "MCFM for the Tevatron and the LHC", *Nucl. Phys. Proc. Suppl.* **205-206** (2010) 10–15, doi:10.1016/j.nuclphysbps.2010.08.011, arXiv:1007.3492.

[15] F. Cascioli et al., "ZZ production at hadron colliders in NNLO QCD", *Phys. Lett.* **B735** (2014) 311–313, doi:10.1016/j.physletb.2014.06.056, arXiv:1405.2219.

[16] F. Caola, K. Melnikov, R. Rntsch, and L. Tancredi, "QCD corrections to ZZ production in gluon fusion at the LHC", *Phys. Rev.* **D92** (2015), no. 9, 094028, doi:10.1103/PhysRevD.92.094028, arXiv:1509.06734.

[17] GEANT4 Collaboration, "GEANT4 – a simulation toolkit", *Nucl. Instrum. Meth. A* **506** (2003) 250, doi:10.1016/S0168-9002(03)01368-8.

[18] CMS Collaboration, "Commissioning of the Particle-Flow Reconstruction in Minimum-Bias and Jet Events from pp Collisions at 7 TeV", CMS Physics Analysis Summary CMS-PAS-PFT-10-002, 2010.

[19] M. Cacciari, G. P. Salam, and G. Soyez, "FastJet User Manual", *Eur. Phys. J. C* **72** (2012) 1896, doi:10.1140/epjc/s10052-012-1896-2, arXiv:1111.6097.

[20] M. Cacciari and G. P. Salam, "Dispelling the N^3 myth for the k_t jet-finder", *Phys. Lett. B* **641** (2006) 57–61, doi:10.1016/j.physletb.2006.08.037, arXiv:hep-ph/0512210.

[21] M. Cacciari, G. P. Salam, and G. Soyez, "The anti-k_t jet clustering algorithm", *JHEP* **04** (2008) 063, doi:10.1088/1126-6708/2008/04/063, arXiv:0802.1189.

[22] CMS Collaboration, "Pileup Removal Algorithms", CMS Physics Analysis Summary CMS-PAS-JME-14-001, 2014.

[23] CMS Collaboration, "Identification of b-quark jets with the CMS experiment", *JINST* **8** (2013) 04013, doi:10.1088/1748-0221/8/04/P04013, arXiv:1211.4462.

[24] Particle Data Group, "Review of particle physics", *Chin. Phys. C* **38** (2014) 090001, doi:10.1088/1674-1137/38/9/090001.

[25] A. Hoecker, P. Speckmayer, J. Stelzer, J. Therhaag, E. von Toerne, H. Voss Collaboration, "TMVA 4, Toolkit for Multivariate Data Analysis with ROOT, Users Guide", Technical Report CERN-OPEN-2007-007, 2009.

[26] CMS Collaboration, "Search for new physics in same-sign dilepton events in proton-proton collisions at $\sqrt{s}$ = 13 TeV", *Eur. Phys. J.C* (2016) doi:10.1140/epjc/s10052-016-4261-z, arXiv:1605.03171. [Erratum: Eur. Phys. J.C76,439(2016)].

[27] J. Campbell, R. K. Ellis, and R. Röntsch, "Single top production in association with a Z boson at the LHC", *Phys. Rev. D* **87** (2013) 114006, doi:10.1103/PhysRevD.87.114006, arXiv:1302.3856.

[28] S. Frixione et al., "Electroweak and QCD corrections to top-pair hadroproduction in association with heavy bosons", *JHEP* **06** (2015) 184, doi:10.1007/JHEP06(2015)184, arXiv:1504.03446.

[29] J. Alwall et al., "The automated computation of tree-level and next-to-leading order differential cross sections, and their matching to parton shower simulations", *JHEP* **07** (2014) 079, doi:10.1007/JHEP07(2014)079, arXiv:1405.0301.

[30] CMS Collaboration Collaboration, "CMS Luminosity Measurements for the 2016 Data Taking Period", Technical Report CMS-PAS-LUM-17-001, CERN, Geneva, 2017.

[31] CMS Collaboration, "Performance of CMS muon reconstruction in pp collision events at $\sqrt{s} = 7$ TeV", *JINST* **7** (2012) P10002, doi:10.1088/1748-0221/7/10/P10002, arXiv:1206.4071.

[32] CMS Collaboration, "Performance of electron reconstruction and selection with the CMS detector in proton-proton collisions at $\sqrt{s} = 8$ TeV", *JINST* **10** (2015) P06005, doi:10.1088/1748-0221/10/06/P06005, arXiv:1502.02701.

[33] CMS Collaboration, "Identification of b-quark jets with the CMS experiment", *JINST* **8** (2013) P04013, doi:10.1088/1748-0221/8/04/P04013, arXiv:1211.4462.

[34] NNPDF Collaboration, "Parton distributions for the LHC Run II", *JHEP* **04** (2015) 040, doi:10.1007/JHEP04(2015)040, arXiv:1410.8849.

[35] ATLAS and CMS Collaborations, "Procedure for the LHC Higgs boson search combination in summer 2011", ATL-PHYS-PUB-2011-011, CMS NOTE-2011/005, 2011.

[36] G. Cowan, K. Cranmer, E. Gross, and O. Vitells, "Asymptotic formulae for likelihood-based tests of new physics", *Eur. Phys. J.C* **71** (2011) 1554, doi:10.1140/epjc/s10052-011-1554-0, 10.1140/epjc/s10052-013-2501-z, arXiv:1007.1727. [Erratum: Eur. Phys. J.C73,2501(2013)].

[37] W. Buchmüller and D. Wyler, "Effective lagrangian analysis of new interactions and flavour conservation", *Nucl. Phys. B* **268** (1986) 621–653.

[38] B. Grzadkowski, M. Iskrzynski, M. Misiak, and J. Rosiek, "Dimension-Six Terms in the Standard Model Lagrangian", doi:10.1007/JHEP10(2010)085, arXiv:1008.4884.

[39] A. Alloul, B. Fuks, and V. Sanz, "Phenomenology of the Higgs effective Lagrangian via FeynRules", *JHEP* **2014** (April, 2014) 110, doi:10.1007/JHEP04(2014)110, arXiv:1310.5150.

[40] J. Ellis, V. Sanz, and T. You, "Complete Higgs Sector Constraints on Dimension-6 Operators", arXiv:1404.3667.

[41] K. Whisnant, J. M. Yang, B.-L. Young, and X. Zhang, "Dimension-six CP-conserving operators of the third-family quarks and their effects on collider observables", doi:10.1103/PhysRevD.56.467, arXiv:9702305.

[42] E. Berger, Q. Cao, and I. Low, "Model independent constraints among the W tb, Z BOSON, and Z BOSON couplings", *Phys. Rev. D* (2009) 1–30, arXiv:0907.2191v2.

[43] R. Röntsch and M. Schulze, "Constraining couplings of the top quarks to the Z boson in ttbar+Z production at the LHC", arXiv:1404.1005.

[44] E. Malkawi and C.-P. Yuan, "Global analysis of the top quark couplings to gauge bosons", *Phys. Rev. D* **50** (Oct, 1994) 4462–4477, doi:10.1103/PhysRevD.50.4462.

[45] C. Zhang, N. Greiner, and S. Willenbrock, "Constraints on nonstandard top quark couplings", *Phys. Rev. D* **86** (July, 2012) 014024, doi:10.1103/PhysRevD.86.014024.

[46] A. Tonero and R. Rosenfeld, "Dipole-induced anomalous top quark couplings at the LHC", *Phys. Rev. D* **90** (July, 2014) 017701, doi:10.1103/PhysRevD.90.017701, arXiv:arXiv:1404.2581v2.

[47] A. Alloul et al., "FeynRules 2.0 - A complete toolbox for tree-level phenomenology", arXiv:1310.1921.